Polytypes and properties of potassium and rare earth double molybdates

Christian Hernández Álvarez[1], Manuel Eulalio Torres Betancort[23] and Mª Cristina González Silgo[23]

[1] *Autor*
[2] *Supervisor*
[3] *Universidad La Laguna, Departamento de Física*

Publication date: September 7, 2021

Abstract—In this Master's Degree Final Project we characterize the crystal structure and dielectric properties of two compounds of the double molybdate family $KRE(MO_4)_2$ (RE = Tb, Yb and M= Mo). The compounds are synthesised by solid-state reaction under different conditions to obtain different crystallographic phases, which were identified by X-ray powder diffraction. Their cell parameters were refined by the Le Bail method: 1) the α-$KEu(MoO_4)_2$ single-phase and the mixture of γ-$KY(MoO_4)_2$ and $RbPr(MoO_4)_2$ phases were obtained for two samples of $KTb(MoO_4)_2$. 2) the majority γ-$KY(MoO_4)_2$ phase was obtained for the sample $KYb(MoO_4)_2$. Dielectric spectroscopy was performed on the single-phase obtained for $KTb(MoO_4)_3$ and conductivity curves were fitted to the Universal Dielectric Response Model. The real part of the electrical permittivity and conductivity showed several anomalies, including the possible α-γ phase-transition. Arrhenius plot and the thermal evolution of the Jonscher parameter were compatible with these anomalies. Possible larger channels in the layered γ-phase than in the α-phase could explain the jump in the electric conductivity. In this family of compounds, the dielectric properties are less studied than the optical ones, so we want to start advancing in the first ones. Furthermore, with a complete knowledge of the phase diagram of this family of compounds, substantial achievements can be made in the field of both solid-state lighting and solid electrolytes.

Keywords—Potassium rare earth double molybdates, scheelite structure, layered structure, phase diagram, polymorphism, solid-state reaction, X-ray powder diffraction, Le Bail refinement, dielectric spectroscopy, Universal Dielectric Response, Arrhenius plot, Jonscher parameter.

Part I
Introduction

Molybdates and double tungstates with formula $ARE(MO_4)_2$ (A=alkali metal, M = Mo, W and RE = rare earth) are materials of great interest, since they are good candidates for applications in different fields: optics, photonics, catalysis, electronics. This condition is because of the varied crystalline structures that give them fascinating crystallochemical and physical properties [1, 2]. In addition, some of these molybdates are known to have non-linear properties (ferroelectric, second harmonic generation) [3]. Furthermore, several recent studies have shown its high photocatalytic activity in the degradation processes of organic compounds and the generation of hydrogen from the separation of water, under UV and visible radiation [4].

The $KRE(MoO_4)_2$ family (RE = rare-earth element) has a great variety of crystalline structures [5] (see Fig.1). Since the structure defines the physical properties [6], the well-known polymorphism converts the $KRE(MoO_4)_2$ family into compounds where research on the structure-property relationship is of very current interest. First of all, $KRE(MoO_4)_2$ compounds are known for their luminescence [7]. Consequently, they can be used 1) as an active medium in solid-state lasers [8] and 2) as phosphors in monochromatic and white light LEDs, depending on the rare earth used or the combination of them [9]. Another interesting aspect that rare earths contribute in double molybdates is the ability to carry out up-/down-conversion processes [10].

Furthermore, the knowledge of the different structural modifications (polymorphs and their phase diagrams) "that can be stable in a crystalline material" is essential to produce nanoparticles of this material [11]. Small differences in enthalpy and free energy between different nanoscale phases offer thermodynamic pathways and related structural mechanisms controlled for possible phase-transitions. Although a crystalline polymorph is thermodynamically the most stable under a given set of conditions (temperature, pressure, oxygen and other gases, electric and magnetic field, etc.), others are often slightly metastable by only a few kilojoules

Contact data: Christian Hdez Álvarez, Chrishdezalvarez@gmail.com

per mole, and different phases can be accesed by specific synthesis routes. For example, the synthesis of lithium ammonium sulfate doped with Er^{3+} and Yb^{3+} had led us to obtain single crystals of the modification α at temperatures between 298 and 313 K, instead of the more favorable and dense ferroelectric phase β [12].

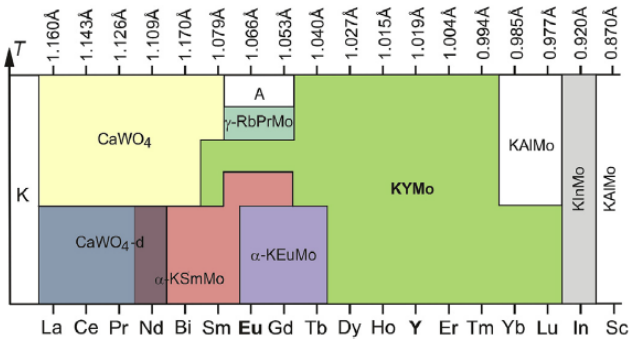

Fig. 1: Structural types of potassium double molybdates, $K^+RE^{3+}(MoO_4)_2$, where R includes rare earths (Sc, Y, La-Lu), Bi e In. The vertical arrow indicates the temperature and the numbers at the top are the ionic radii of the ions RE^{3+} for the coordination of O^{2-} [13].

Moreover, the electrical properties of the double and triple molybdates have attracted great attention because some of them have a high ionic conductivity of the alkaline metal (Na^+ and K^+), Ag^+ or Tl^+ [14]. The molybdates with the NASICON structure (sodium superionic conductors $Na_3Zr_2Si_2PO_{12}$ with space group $R\bar{3}c$ [15]) are particularly interesting; from the ionic transport point of view. This structural type has been proved for the first time in molybdate with the formula: $Na_{2x}M_2Sc_{2-x}(MoO_4)_3$ (with M = Zn, Cd or Mg) [16]. Compounds with potassium, for example, $KMgIn(MoO_4)_3$ has been determined that between the temperature range from 293 to 873 K the conductivity can increase up to 6 orders of magnitude, reaching up to $7x10^{-3}$ S/cm. This compound has a monoclinic structure that can be considered a distortion of the NASICON structure [17]. More recently, the structure and ionic conductivity of triple molybdates have been studied with the formula: $K_5RZr(MoO_4)_6$ (R = Al, Cr, Fe, In, Sc) where it has been obtained that the electrical parameters present anomalies between 700 and 900 K due to a first order phase-transitions and that the electrical conductivity increases up to 6 orders of magnitude (reaching values between 10^{-2} and 10^{-3} S/cm). These compounds crystallize in the hexagonal system with space group $P6_3$, similar to the structure of NASICON with channels of large cross-section. Alkali potassium cations are found within large polyhedra and authours explained that this structure favors their mobility [18, 19].

It is more difficult to find studies of electric conductivity in double molybdates, specifically with potassium. The electrical conductivity increases in $K_2Sr(MoO_4)_2$ by a factor of 10 around 744K when the distorting phase-transition β-γ occurs. There is a substantial improvement in the mobility of the potassium ion associated with a change in conductivity pathway from quasi-one-dimensional to two-dimensional [20]. The high-temperature γ-phase corresponds to the most symmetric palmierite-type phase with space group $R\bar{3}m$. The study of double molybdates with this structure and the formula: $K_5R(MoO_4)_4$ (R = trivalent element) also show a remarkable mobility of K^{+1} ions (up to 10^{-3} S/cm) in the directions parallel to the layers of the framework. In this type of compounds, it is observed that the occupations of the non-equivalent positions of the potassium ions change from ordered type to statistical disorder with increasing temperature, which indicates the possibility of moving large cations from one position to another [21].

In relation to the stoichiometry that we are studying, there are practically no references of dielectric studies. However, we have to add that, during the preparation of this TFM, they have note two works have been published about the compounds $KTb(MoO_4)_2$ and $KYb(MoO_4)_2$ [22, 23]. In the first, the influence of different synthesis routes on the structure and luminescent properties of $KTb(MoO_4)_2$ was investigated. The two possible phases were prepared by solid-state, hydrothermal and Czochralski techniques. These methods gave rise to the triclinic (space group $P\bar{1}$) phase α-$KEu(MoO_4)_2$ (by solid state synthesis), and the orthorrombic (space group Pbcn) phase γ-$KY(MoO_4)_2$ (by hydrothermal and Czochralski synthesis). Furthermore, the electrical conductivity was measured confirming the possibility of migration of the K^+ cations, located in extensive two-dimensional channels along the crystallographic axes c and a. In the case of $KYb(MoO_4)_2$, crystals grew by spontaneous nucleation from a flow of $K_2Mo_4O_{13}$ in the $KY(MoO_4)_2$ phase. The Raman spectra and magnetic susceptibility were also analyzed.

I. Motivations.

The CCDD (Crecimiento, caracterización y difracción de materiales dieléctricos) group takes many years studying the family of compounds with formula $RE_2(MO_4)_3$ with M = Mo and W with a large polymorphism and interesting optical and electrical properties related to its structural variety. This research group has studied the phase diagram of this whole family in different experiments varying the temperature and pressure. The family of double molybdates with potassium also presents a complex phase diagram (Fig.1) that is less studied, so they have begun to synthesize compounds that belong to zones where several polymorphs are possible. In particular, terbium potassium and ytterbium potassium double molybdates have been chosen. The first one shows different environments for the Tb ion, which affects its green emission in the field of (down-conversion) [24]. In the case of Yb double molybdate, we also look for different polymorphs where different environments for Yb, could affect the up-conversion when co-dopants such as (Er and/or Tm) are used. Although these optical applications may be of great interest, they will not be the focus on this work. Before that, we have to get the pure phases, it is not usually easy to obtain them because the transition temperatures are unknown. A very laborious synthesis is expected, but we like the challenge. If we achieve these phases, we are interested in their structural and electrical-dielectric characterization, these properties are much less studied. Moreover, dielectric permittivity will allow us to know the stability of the polymorphs. The different phases must have different conductivities (3D structures, layers...). It is

expected that if rare earth layers are formed, with greater distances between them, there will be wider channels for the conduction of potassium ions.

The situation that arose due to COVID-19 and the problems with SEGAI personnel (General Research Support Services of the ULL [25]), make us prioritize the work in the Low Frequency Laboratory where we can perform synthesis and dielectric measurements. It would be desirable to have thermal analysis measures, but we did not collect them.

II. Objectives.

The objectives set for this TFM are:

1. Synthesize for the first time the compounds $KTb(MoO_4)_2$ and $KYb(MoO_4)_2$ with different solid-state synthesis routes in order to obtain different pure polymorphic phases.

2. Identify phases for two compounds: $KTb(MoO_4)_2$ and $KYb(MoO_4)_2$, starting from the phase diagram shown in Fig.1. We hope to find new polymorphs in zones where 3D structures coexist with layered structures.

3. Refine the X-ray diffractograms starting from known structures or introducing small distortions. If pure phases are not obtained, we will also refine the mixture of phases. We will be able to obtain the crystallographic cell parameters from the refinement and corroborate the crystal structure (space group and atomic positions).

4. In the case of obtaining pure phases, we will perform the dielectric characterization by means of impedance spectroscopy as a function of temperature and frequency. We will analyze the possible phase-transitions from the behavior of the permittivity and the electrical conductivity.

5. We will correlate the crystal structure with the results of the dielectric properties. We will study the differences between 3D structures and layered structures and how RE^{3+} and K^{+} cations are arranged in them to contribute to thermal, photocatalytic and luminescent properties, but specially dielectrical and electrical ones.

III. Work Organization.

The introduction of the TFM consists of a complete bibliographic review to show a state of the art that emphasizes the current interest that the $KRE(MoO_4)_2$ family has. We have reviewed its main properties emphasizing the electrical ones. Within the introducction, we have dedicated three sections to the motivations that have inspired this work, the specific objectives and how we have organized the writing.

The methodology consists of four sections to describe the experimental procedure. We will write a small summary of each technique, the physical foundations and the experimental conditions. Thus, the first section deals with the solid-state reactions of the studied compounds, the second on X-ray diffraction in polycrystalline samples and the third on dielectric spectroscopy in pure phases. The last section is dedicated to the description and comparison of the crystalline structures that belong to the phase diagram to facilitate the analysis.

In the section "Results and Discussion," we will begin by explaining how the data are analyzed to facilitate the discussion. In the case of X-ray diffraction, we will describe how the phase identification is performed from routine diffractograms to Le Bail refinement. We will also explain some strategies followed to achieve better results. In the case of dielectric spectroscopy we will describe the analysis of the data in the context of the Universal Dielectric Response Theory. Finally, we will discuss the results obtained with both techniques and we will relate them.

The last section will consist of a compendium of the conclusions of the TFM and we will end by presenting our vision of the possible future work in order to continue and improve the research in this family of compounds.

Part II
Metodology

IV. Synthesis method.

The synthesis method used is the solid-state reaction (ceramic method) which consists of the reaction of the starting reagents at high-temperatures and during a relatively long heating time. It can allow the reagents to diffuse for shaping the desired single-phase.

This method has been, for many decades, the most widely used in the preparation of materials. However, it has been shown to offer several drawbacks:

1. Intergranular and intragranular diffusion problems: Consider that we want to obtain compound C from reactants A and B, that is: $A + B \rightarrow C$.

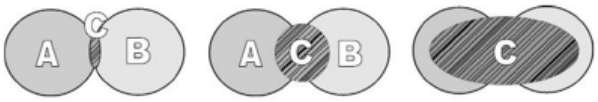

Fig. 2: Inter and intragranular diffusion processes.

Compound C gives rise to problems of counterdiffusion of ions A and B through the interface. As the reaction progresses, this increase lead to the reaction speed decreases due to the greater distance between reactives Fig.2. The problem can be solved with intermediate grinding during the different heating phases.

2. Obtaining the single-phase C: It is not always possible to obtain a pure compound (only one phase), this may be due to:

- During treatment at high-temperatures, some of the reagents may become sublimated.

- Large size of the reagent grains (improper grinding and/or bonding between grains, leading to a larger grain size).

The evolution of this process (obtaining the single-phase) must be followed by X-ray Diffraction. The experimental procedure is the one indicated in Fig.3.

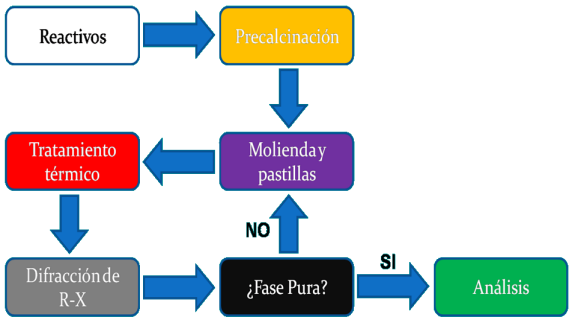

Fig. 3: Experimental procedure.

V. Sample Preparation.

All the experiments, except for the X-ray diffraction, were carried out in the Low Frequency Laboratory of the University of La Laguna. The code indicated in Table 1 indicates the different syntheses.

a. Synthesis of $KYb(MoO_4)_2$.

The synthesis of 1g of potassium ytterbium molybdate [$KYb(MoO_4)_2$] was carried out from the reactives: potassium carbonate (K_2CO_3), molybdenum oxide (VI) (MoO_3) and ytterbium (III) oxide (Yb_2O_3) in stoichiometric proportions. In Table 2 indicates the corresponding molecular weight, given by the manufacturer (Aldrich) for each reagent (*all the starting reactives have a purity of 99.99 %*).

It should be noted that for the adjustment of the reaction equation (A + B + C → D + by-products), the thermal decomposition of potassium carbonate must be taken into account (CO_2 is released).

The balanced equation is:

$$4MoO_3 + K_2CO_3 + Yb_2O_3 \rightarrow$$
$$2KYb(MoO_4)_2 + CO_2 \quad (1)$$

TABLE 2: Amounts of compounds for 1g of $KYb(MoO_4)_2$.

Compound	PM (g/mol)	Mass (g)	Mass (obtain 1g) (g)
MoO_3	143.9382	575.7528	0.5411
K_2CO_3	138.2055	138.2055	0.1299
Yb_2O_3	394.0782	394.0782	0.3704
$KYb(MoO_4)_2$	532.0135	1064.027	1
CO_2	44.0095	44.0095	0.0414

According to previous experiences (see Supplementary information Part VII, Section XV) to obtain 1g of the $KYb(MoO_4)_2$, it is necessary to use an extra percentage of the reactives calculated above (Table 3). These quantities will be precalcined following the heat treatments indicated below.

TABLE 3: Amounts of reagents required.

Reactives	Mass (obtain 1g) (g)	Extra Percentage (%)	Final Mass (g)
MoO_3	0.5411	10	0.5952
K_2CO_3	0.1299	30	0.1689
Yb_2O_3	0.3704	10	0.4074

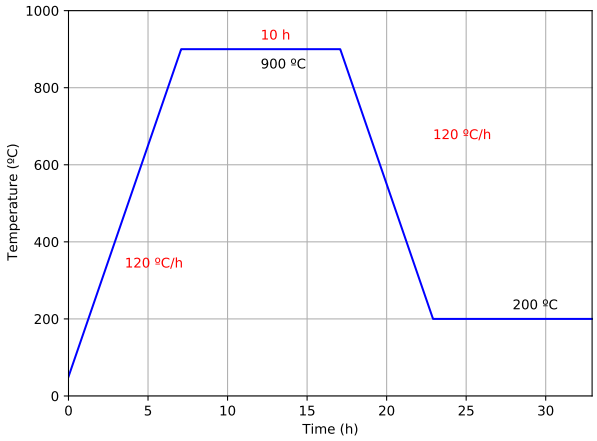

Fig. 4: Precalcination of rare earth oxides. This treatment is common for all rare earth oxides.

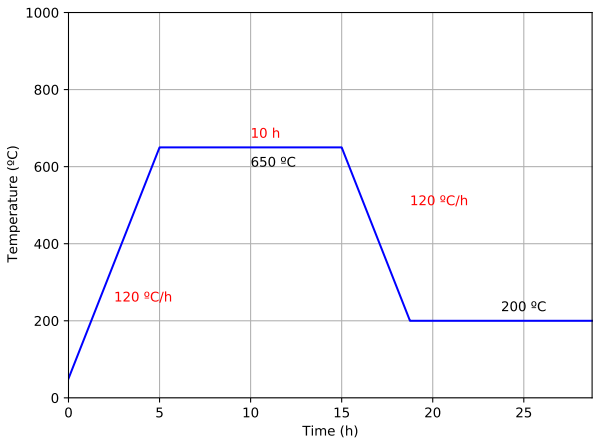

Fig. 5: Precalcination of the reactive (MoO_3).

The necessary amount of reagents was weighed (previous precalcination, following the heat treatments shown in Figs. 4, 5 and 6).

Then, these reagents were grounded in an agate mortar and for at least 1 hour, so that the mixture was as homogeneous as possible (during process, it is convenient to add a small amount of acetone to promote mixing). In all cases, pellets were obtained from ground powder to increase the contact surface between the grains, thus favoring the reaction. And then the pellets were placed in a platinum crucible and subjected to a heating/cooling program (Fig.7). The process was supervised by X-ray Diffraction until the desired single-phase was obtained.

TABLE 1: Compound Synthesis: Codes

Codes	Obtain	Temperature(ºC)	Time(h)	Pressure(ton)	Supplementary information
M0a	$KYb(MoO_4)_2$	700	90	3	Part VII, Section XV - a
M0a	$KYb(MoO_4)_2$	725	90	3	Part VII, Section XV - b
M1	$KYb(MoO_4)_2$	680	90	3	Part VII, Section XV - c
M2	$KYb(MoO_4)_2$	680	90	3	Part VII, Section XV - c
M3	$KYb(MoO_4)_2$	725	90	5	Part VII, Section XV - c
M4	$KYb(MoO_4)_2$	725	90	5	Part VII, Section XV - c
M5	$KYb(MoO_4)_2$	680	90	3	Part VII, Section XV - d
M6	$KYb(MoO_4)_2$	680	90	5	Part VII, Section XV - d, g
M7	$KYb(MoO_4)_2$	750	90	3	Part VII, Section XV - d
M8	$KYb(MoO_4)_2$	750	90	5	Part VII, Section XV - d
M9	$KYb(MoO_4)_2$	625	90	3	Part VII, Section XV - e
M10	$KYb(MoO_4)_2$	625	90	5	Part VII, Section XV - e
M11	$KYb(MoO_4)_2$	650	90	3	Part VII, Section XV - e
M12	$KYb(MoO_4)_2$	625	60	3	Part VII, Section XV - e
M13	$KYb(MoO_4)_2$	690	90	3	Part VII, Section XV - f
M14	$KYb(MoO_4)_2$	700	90	3	Part VII, Section XV - f
M15	$KYb(MoO_4)_2$	710	90	3	Part VII, Section XV - f
$KTb(MoO_4)_2$ baja	$KTb(MoO_4)_2$	700	80	3	
$KTb(MoO_4)_2$ alta	$KTb(MoO_4)_2$	850	80	3	

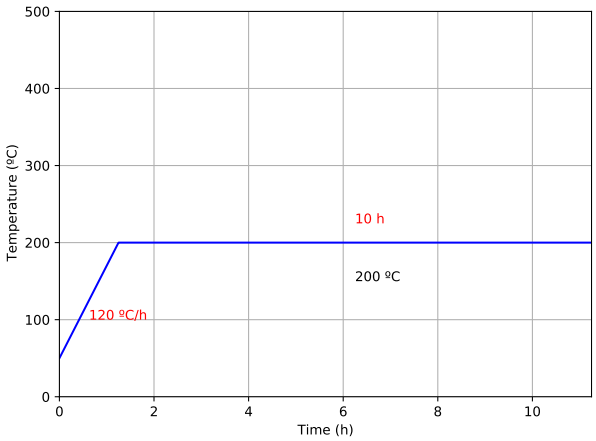

Fig. 6: Precalcination of the reactive K_2CO_3.

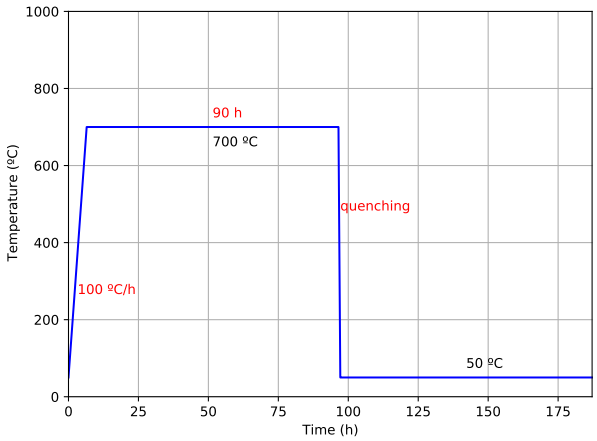

Fig. 7: Heat treatment to obtain the $KYb(MoO_4)_2$.

b. Synthesis of $KTb(MoO_4)_2$ phases.

The synthesis of 1g of potassium terbium molybdate [$KTb(MoO_4)_2$] was carried out from the reagents: potassium carbonate (K_2CO_3), molybdenum oxide (VI) (MoO_3) and terbium (III, IV) oxide (Tb_4O_7) in stoichiometric proportions. Table 4 indicates the corresponding molecular weight, given by the manufacturer (Aldrich) for each reagent (*all the starting reactives have a purity of 99.99 %*).

The equation adjusted with the coefficients obtained was as follows:

$$16MoO_3 + 4K_2CO_3 + 2Tb_4O_7 \rightarrow$$

$$8KTb(MoO_4)_2 + 4CO_2 + O_2 \qquad (2)$$

TABLE 4: Amounts of reagents for 1g of $KTb(MoO_4)_2$.

Compound	PM (g/mol)	Mass (g)	Mass (obtain 1g) (g)
MoO_3	143.9382	2303.0112	0.5558
K_2CO_3	138.2055	552.8220	0.1334
Tb_4O_7	747.70	1495.4	0.3609
$KTb(MoO_4)_2$	517.92	4143.36	1
CO_2	44.0095	176.038	0.0425
O_2	31.9988	31.9988	0.0077

As for the potassium and ytterbium molybdate, to obtain 1g of $KTb(MoO_4)_2$ we used an extra percentage of the reagents calculated above (Table 5). These amounts were precalcined following the same heat treatments of Figs. 4, 5 and 6. After precalcination, the same procedure was followed as with $KYb(MoO_4)_2$, then it was subjected to a heat treatment (see Fig.7) and then the process was monitored by means of X-ray diffraction until obtaining the desired single-phase.

TABLE 5: Amounts of reagents required.

Reactives	Mass (obtain 1g) (g)	Extra Percentage (%)	Final Mass (g)
MoO_3	0.5558	10	0.6114
K_2CO_3	0.1334	20	0.1601
Tb_4O_7	0.3609	10	0.3970

VI. X-ray Powder Diffraction.

X-ray diffraction measurements were carried out to confirm and characterize the samples. This physical phenomenon occurs when a wavefront encounters an obstacle comparable in size to its wavelength (X-rays have wavelengths on the same order of interatomic distances). The diffracting obstacle (crystal lattice) becomes a secondary source of the scattered waves. Differences among the optical paths and the initial phase produce constructive or destructive interferences among secondary waves with even or odd multiple of π phase shift. A diffraction pattern consists of a plot of the scattered intensity versus the diffraction angle.

Bragg's law appears from the discoveries of William Henry Bragg and his son William Lawrence Bragg in 1913 [26]. They concluded that X-ray diffraction geometry was similar of a ray of light striking a plane mirror. It is considering a crystalline structure is formed by families of equispaced parallel planes that contain identical atomic arrangements. The incident beam forms an angle θ with a set of these planes. Thus, the reflected beam will also form an angle θ with these planes and the resulting angle between the two beams will be 2θ. There are many families of planes within a crystal. The reflections produced in each family of planes interfere with each other. This interference will be constructive when the difference in optical paths between the reflected beams from consecutive planes is equal to an integer multiple of the wavelength (see Fig.8).

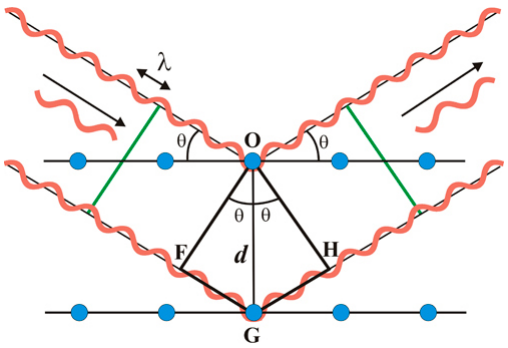

Fig. 8: Bragg's Law Diagram [27].

Bragg's law (Eq.3) allows predicting the angles 2θ at which the X-rays are diffracted, where n is an integer, d is the distance between the crystal lattice planes, and λ is the wavelength of the incident ray. As X-rays have a great penetrating power, this phenomenon is not limited to the surface planes of the sample [27].

$$2dsin(\theta) = n\lambda \tag{3}$$

A diffractometer is an instrument that allows measuring the diffraction of an X-ray beam (or of neutrons or electrons) when it intercepts a crystalline sample. Schematically, a diffractometer consists of an x-ray generator tube, a platform to place the sample and a detector, as well as a series of optical elements (primary and secondary optics) that allow: 1) the beam to be collimated, 2) reduce the scattering of the rays, and 3) ensure that the incident and diffracted beam present an appropriate section [28].

The structural characterization has been carried out using crystalline powder X-ray diffraction at SIDIX (Integrated X-ray Diffraction Service [29]), which is part of the General Research Support Services of the ULL (SEGAI [25]). The service has a powder diffractometer. In this equipment, the X-ray source consists of a Cu anode that generates characteristic wavelengths CuK_α and CuK_β, from which the first is selected with a Ni filter. In turn, the radiation is composed of two lines named: $K_{\alpha1}$ and $K_{\alpha2}$ with wavelengths: 1.54056 Å and 1.54443 Å, respectively. The detector that collects the diffracted light intensity usually is an area detector.

The geometry used in the diffractometer is that of Bragg-Brentano, a configuration that detects the beam diffracted by the sample in reflection mode (it could be in transmission mode). To do this, the angle of incidence varies by rotating the sample an angle θ and the detector an angle 2θ. The source and detector trace a path on the circumference of a circle with its axis on the specimen surface. The equipment used for the measurements was the Malvern Panalytical "Empyream" diffractometer. Our routine measurements were carried out using a continuous scan in the angular interval $5º<2\theta<80º$ in steps of 0.03º with an integration time of approximately 60s. In Fig.9 the different elements used can be distinguished: (I) X-ray generator, (II) goniometer, modifies the angle of incidence 2θ in the range from -111º to 168º, (III) optical elements [a) 1/8º divergence slit (primary and secondary), b) mask to limit the beam width (primary), c) soller slits of 0.04 rad, it is a set of sheets that eliminate the angular divergence of the beam so that it reaches the sample as parallel as possible (primary), d) antiscattering slit of ½º to eliminate scattered radiation (secondary)], (IV) sample platform, where the sample holder is placed for the measurement, (V) Pixel1D detector with Medipix3 technology, (VI) sample exchanger, which allows programming several continuous measurements with different parameters in each case: angular interval, integration time, etc.

This equipment allows different sample holders depending on the type of measurement to be carried out and the amount of sample. In our case, the low-background specimen holder (Fig.10a) of approximately 1 mm deep were used, for a small sample; and zero-background sample holder (Fig.10b), with about 50 microns, for a very small amount of sample. During assembly, it is necessary to avoid the preferential orientation of the crystals, making circular movements favoring the random orientation; otherwise an error is introduced in the intensity of the diffraction peaks.

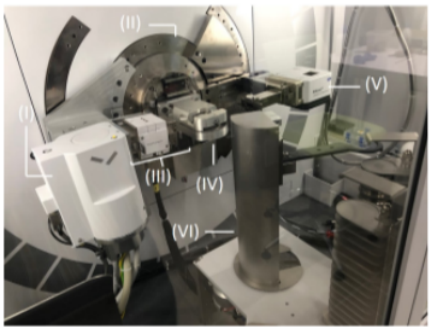

Fig. 9: Diffractometer Empyrean of Malvern Panalytical.

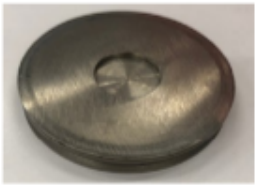

(a) Low-background-specimen-holder (LBH)

(b) Zero-background sample holder (ZBH)

(c) Example of sample mounted on ZBH

Fig. 10: Types of sample holders.

VII. Dielectric Spectroscopy.

The Dielectric Spectroscopy studies the response of materials when a time-varying electric field is applied to them. This response is expressed in terms of a macroscopic and complex magnitude, the dielectric permittivity (ε), the analysis of ε as a function of temperature and frequency gives microscopic information.

There are several different dielectric mechanisms, related to how the medium under study responds to the applied field. Each dielectric mechanism has a characteristic frequency, which is the reciprocal of the characteristic time of the process. In general, dielectric mechanisms can be divided into relaxation and resonance processes. In Fig.11 the main dielectric processes are shown depending on the frequency.

We can also obtain information about electrical conductivity, a physical property that reflects the ability of matter to transfer electrical charge. The conductivity is related to the electrical permittivity, understood as the ability of a material to polarize under the action of an electric field. In salts, conductivity is due to ion mobility, which depends on many factors: the size of the ions and the strength of the ionic bonds. The electrical conductivity of solid compounds has received considerable attention recently. Nowadays, initial demand for: electrically insulating materials, semiconductors, metallic conductors, and superconductors has

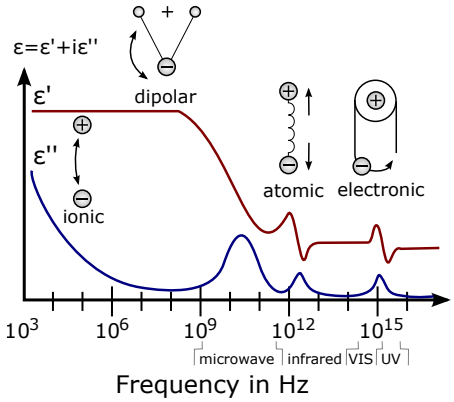

Fig. 11: A spectrum of dielectric permittivity over a wide range of frequencies. The real and imaginary parts of the permittivity are shown, and various processes are represented: ionic and dipole relaxations, and atomic and electronic resonances at high energies [30].

now expanded to include ionic superconductors.

In materials science, fast ionic conductors are solids in which the ions are highly mobile. These materials are essential in the field of solid-state ionics. These materials are useful in batteries and various sensors. Fast ionic conductors are primarily used in solid oxide fuel cells where solid electrolytes allow the movement of ions without the need for a liquid or soft membrane separating the electrodes. The phenomenon is based on the jump of ions through a rigid opposite structure [31].

Materials for electrical applications must guarantee a homogeneous behavior, regardless of external conditions (temperature, humidity, etc.) during a long useful life. In addition, its manufacturing process must be inexpensive. All these factors motivate the industry to look for new materials to replace the traditional ones (iron, copper, gold, etc.). From the point of view of industrial applicability, materials with dielectric properties that exhibit predictable and uniform thermal behavior are in high demand. In this sense, ionic crystals have shown good stability due to their low number of crystal defects at room temperature. However, at higher temperatures, more defects occur, in turn increasing the conductivity. The initial number of defects depends on the crystal growth technique used, and the inclusion of dopants in the crystal composition [32].

The dielectric characterization has been carried out with an impedance analyzer "HP 4192A F" in the Low-Frequency Laboratory of the University of La Laguna. This equipment (Fig.12) allows measuring the impedance of electronic components, telecommunications filters and image and audio circuits.

In this work, pellets of each compound (pure phases) were measured and its dielectric permittivity was obtained in a determined range of frequencies, applying an alternating voltage and in a given range of temperatures.

In order collect data at different temperatures, the sample was placed in an oven (Fig.13). Before starting to mea-

Fig. 12: Impedance measurement equipment: HP 4192A LF Impedance Analyzer.

sure, it is necessary to calibrate the equipment and collect some pellet measurements to use in the equipment software. For the samples that were synthesized before measuring, the equipment was programmed with several parameters, among which the equipment requests the C_a (Active Capacity) that depends on the dimensions of the pellet (Fig.14).

Fig. 13: Oven used to heat the sample during impedance spectroscopy testing.

$$C_a = \varepsilon_o \frac{A}{e} \tag{4}$$

Where ε_o is the permittivity of the vacuum, A is the electrode area and e is the thickness of the pellet.

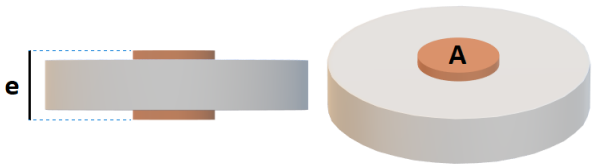

Fig. 14: Pellet dimensions.

- Experimental conditions for $KTb(MoO_4)_2$: A frequency range of 5 Hz to 13 MHz, an alternating voltage of 1 V and a temperature range of 323 K to 873 K with steps of 5K, with a warming and cooling rate of of 50K/h. C_a = 0.43 pF.
- Experimental conditions for $KYb(MoO_4)_2$: A frequency range of 5 Hz to 13 MHz, an alternating voltage of 1 V and a temperature range of 323 K to 923 K with steps of 5K, with a warming and cooling rate of of 50K/h. C_a = 0.25 pF. This sample could not be studied since the equipment broke down during the measurement.

VIII. Phase Diagram of $KRE(MoO_4)_2$ family

This section describes phase diagram of Fig.15. We will compare the different phases that correspond to high and low-temperatures in order to be able to interpret the changes in dielectric properties with temperature.

a. Comparison between the scheelite structure and the α-$KEu(MoO_4)_2$ structure.

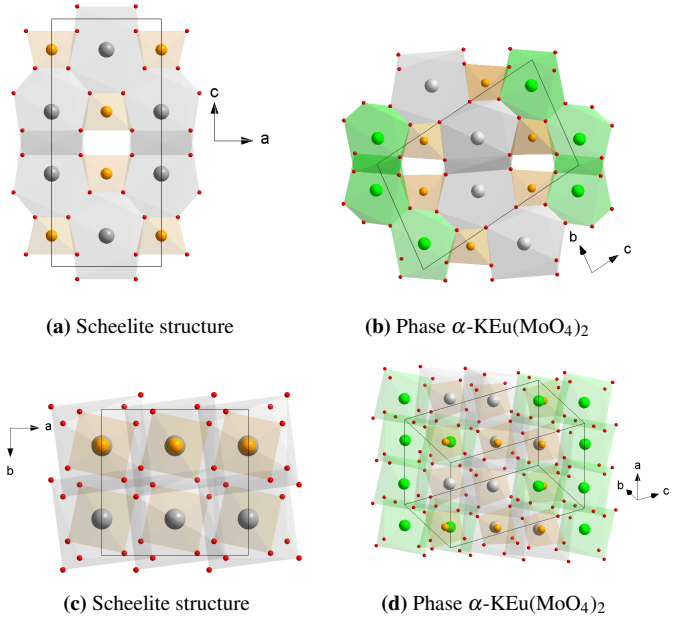

(a) Scheelite structure **(b)** Phase α-$KEu(MoO_4)_2$

(c) Scheelite structure **(d)** Phase α-$KEu(MoO_4)_2$

Fig. 15: Projection of structures of $KRE(MoO_4)_2$ perpendicular to different directions. Mo atoms are drawn orange, RE atoms green, K atoms gray and O atoms red.

The scheelite structure was found for the first time in $CaWO_4$ [33]. It is built in two columns [...-AO_8-MO_4-...] along the c axis (see Fig.15c). The AO_8 polyhedron and the MO_4 tetrahedron form a 3D network sharing common vertices. The cations A and/or B can be partially substituted in the form $(A',A'')_n[(M',M'')O_4]_m$ (A´, A" = alkaline, alkaline earth or rare earth and M´, M" = Mo, W). The substitution of Ca^{2+} by a combination of M^+ (Li^+, Na^+, K^+, Ag^+) and a trivalent cation allows the formation of the double molybdates $MRE(MoO_4)_2$ (RE = rare earth, Y, Bi).

Double molybdates $KRE(MoO_4)_2$ family owns various polymorphic structures, as seen in Fig.1, which can be divided into scheelite-type modifications (RE = La-Dy) and non-scheelite modifications. (RE = Dy-Lu) [34]. Within the scheelite-type there are three subgroups: 1) tetragonal

scheelites (RE = La-Sm) with space group $I4_1/a$, monoclinic phases with a small distortion of the scheelite structure (called $CaWO_4$-d) are in this group. 2) phases with incommensurable modulated structure (RE = Nd and Sm) with superspace group $I2/b(\alpha\beta 0)00$). 3) Triclinic phases with the structure-type α-$KEu(MoO_4)_2$ and space group $P\bar{1}$; in contrast to the tetragonal scheelite phase where the K and RE cations are statistically distribute in the phase α-$KEu(MoO_4)_2$ are ordered (Fig.15b). The K and RE cations are partially ordered in the incommensurate structure [5, 34].

b. Comparison between the structure α-$KEu(MoO_4)_2$ and the structure γ-$KY(MoO_4)_2$.

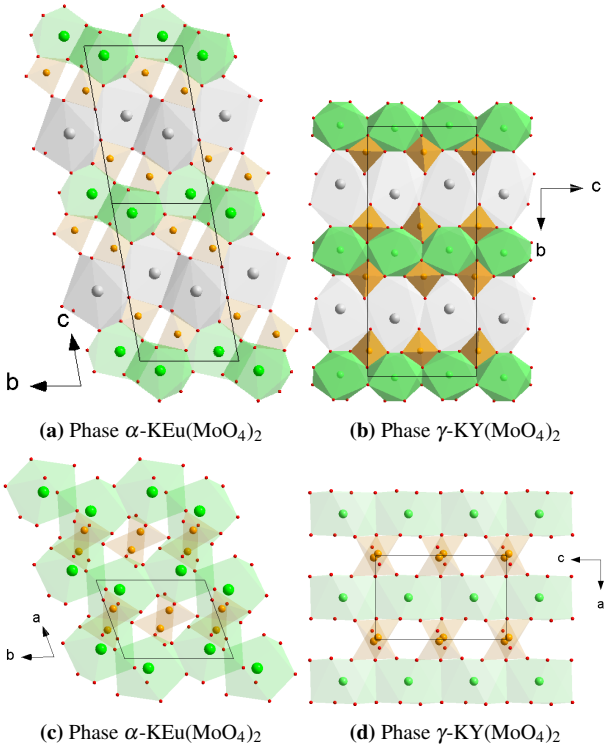

(a) Phase α-$KEu(MoO_4)_2$ **(b)** Phase γ-$KY(MoO_4)_2$

(c) Phase α-$KEu(MoO_4)_2$ **(d)** Phase γ-$KY(MoO_4)_2$

Fig. 16: Projection of structures of $KRE(MoO_4)_2$ with perpendicular view to different directions. Mo atoms are drawn orange, RE atoms green, K atoms gray and O atoms red. In (c) and (d), only the YMo_2O_8 layers have been drawn without potassium atoms for a better viewing.

In the group of non-scheelite modifications, the orthorhombic phase of the $KY(MoO_4)_2$ type is a layered structure, as shown in Fig.16a. It contains $[YMo_2O_8]$ layers formed by MoO_4 tetrahedra and YO_8 polyhedra, which are perpendicular to the *b*-axis. A layer of K^+ separates two neighboring layers of $[YMo_2O_8]$ in a zigzag way. Two YO_8 polyhedra share an O-O edge and form infinite $[Y_2O_{14}]$ n chains. The MoO_4 tetrahedra separate the neighboring $[Y_2O_{14}]_n$ chains. Thus, the ordering of Y^{3+} in phase γ is 1D. In the zigzag K^+ layer, each K^+ ion is surrounded by six other K^+ ions [22, 23]. The difference between the α-$KEu(MoO_4)_2$ and γ-$KY(MoO_4)_2$ structures can be better understood by considering the rare earth environment RE^{3+} and its neighbors RE^{2+} (Fig.16c, d). In phase γ the layer of lanthanide ions is a flat layer in which each cation is surrounded by four cations of the same type, forming a perfect rectangular lattice. In the phase α, six RE^{3+} cations form six-membered rings. We can also consider a layer of RE^{3+} cations built from these rings resulting in a 2D network of RE^{3+}. However, it is not a perfectly flat layer. The zigzag K^+ layer of phase γ is more similar to that of phase α. In the phase α, the layers of the cations RE^{3+} and K^+, form six-membered rings as the phase γ [22]. This narrowing of the entire layer $[YMo_2O_8]$ within the phase γ can allow conduction channels of potassium K^+ ions along with the directions *a* and *c*, comparing the phase α.

c. Comparison between the structure structure γ-$KY(MoO_4)_2$ and the structure $RbPr(MoO_4)_2$.

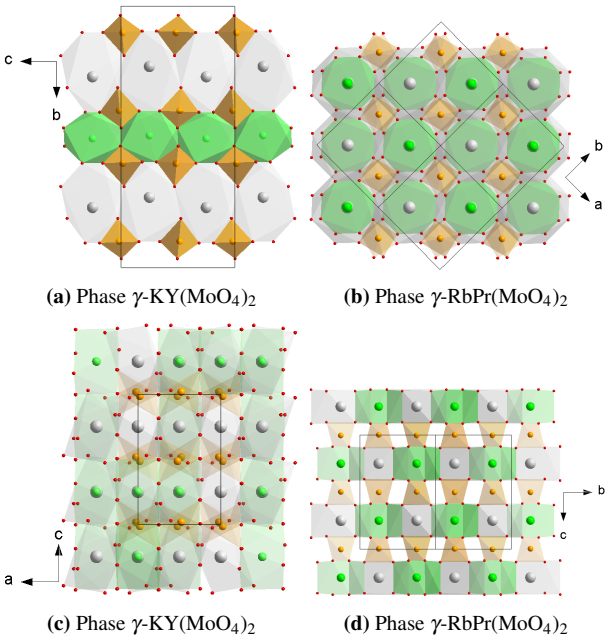

(a) Phase γ-$KY(MoO_4)_2$ **(b)** Phase γ-$RbPr(MoO_4)_2$

(c) Phase γ-$KY(MoO_4)_2$ **(d)** Phase γ-$RbPr(MoO_4)_2$

Fig. 17: Projection of structures of $KRE(MoO_4)_2$ with perpendicular view to different directions. Mo atoms are drawn orange, RE atoms green, K atoms gray and O atoms red.

This type of structure was initially observed for γ-$RbPr(MoO_4)_2$ [35]. This phase has a space group P4/nnc or Pnnn. Its structure is built with tetragonal antiprims of PrO_8 and RbO_8 joined through shared lateral edges and alternating in "checkerboard" order, as illustrated in Fig.17d. The Rb and Pr layers share oxygen vertices with the intercalated MoO_4 tetrahedra providing interlayers bonding.

Part III
Results and Discussion

IX. Phase Identification.

Theoretical diffractograms of $KRE(MoO_4)_2$ phases are the starting point for identifying synthesized crystalline phases. These patterns are calculated from the corresponding ".cif" files (crystallographic information file, obtained from the ICSD database [36]). In order to detect possible impurities caused by the reagents that have not reacted during the synthesis process, the measured diffractograms are represented together with the theoretical ones. Both patterns are com-

pared by using the WinPLOTR [37] computer program. To facilitate the writing and handling of the data, we use the codes indicated in Table 1.

a. Potassium ytterbium double molybdates.

Diffractograms M5-M12 could correspond to a mixture of phases (see Figs. 18 and 19): 1) the majority phase with the structure γ-$KY(MoO_4)_2$ (kYb(moo4)2-faseY), and 2) the minority phase with the hydrated structure γ-$Sc_2(WO_4)_3$ (gamma_Y). The hydrated phase γ-$Sc_2(WO_4)_3$ is not resolved, but we have raw data of a sample of $Y_2(MoO_4)_3$ to compare. In addition, Bragg peaks of the theoretical non hydrated phase γ-$Sc_2(WO_4)_3$ (fasegamma_hkl) were obtained from the ICSD database.

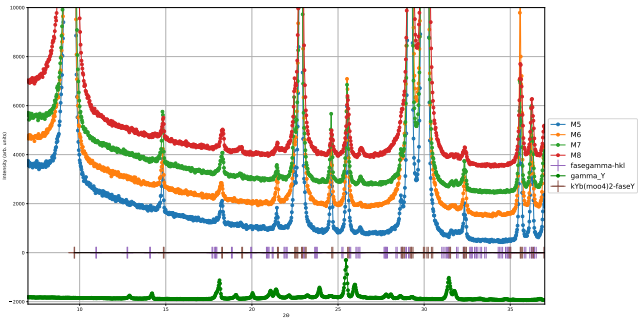

Fig. 18: Diffractograms M5-M8 and $Y_2(MoO_4)_3$ (raw data). The bars correspond to the Bragg reflections of the phases γ-$KY(MoO_4)_2$ and of the γ-$Sc_2(WO_4)_3$ (not hydrated).

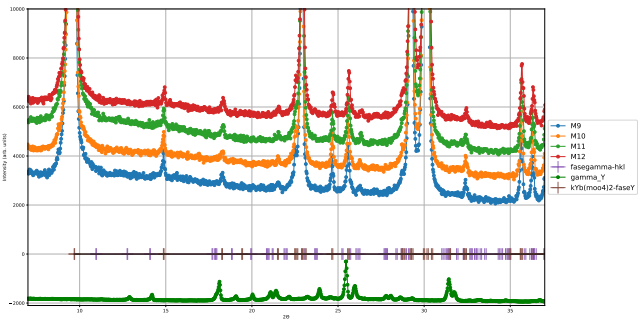

Fig. 19: Diffractograms M9-M12 and $Y_2(MoO_4)_3$ hydrated (raw data). The bars correspond to the Bragg reflections of the phases γ-$KY(MoO_4)_2$ and of the γ-$Sc_2(WO_4)_3$ (not hydrated) .

Regarding the M1, M2 and M3 diffractograms (see Fig.20), we have represented them together with: 1) the majority γ-$KY(MoO_4)_2$ phase (kYb(moo4)2-faseY), 2) the theoretical reflections of the oxides of potassium, molybdenun (K2O, MoO3) and 3) the K_2MoO_4 reflections. In the case of the M4 diffractogram, K_2MoO_4 can be detected as an impurity, however the oxides are not easy to detect.

b. Potassium terbium double molybdates.

The low-temperature phase is perfectly identified with the triclinic phase of $KEu(MoO_4)_2$ (KTb(MoO4)2_Baja), note the blue diffractogram of Fig.21. However, we expected the phase γ-$KY(MoO_4)_2$ (KTb(MoO4)2_Alta) for the sample prepared at high temperature (orange diffractogram in Fig.21). This phase appears with other quite intense peaks. The peak at the lowest angle (2Θ = 8º) corresponds

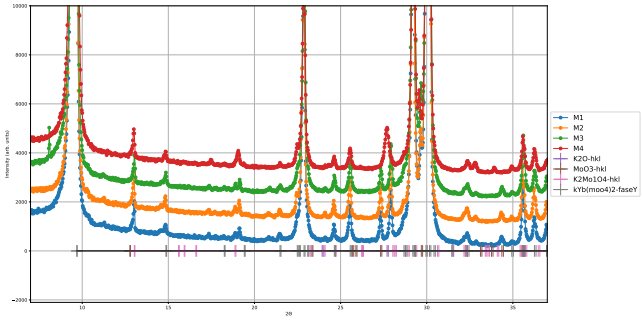

Fig. 20: Diffractograms M1-M4 (raw data). The bars corresponding to the Bragg reflections of the phases γ-$KY(MoO_4)_2$, of the oxides K_2O and MoO_3, and of K_2MoO_4).

to the phase $KEu(MoO_4)_2$ that coexists with the phases $KY(MoO_4)_2$ as discussed in the bibliography [22, 23]. However, other peaks also appear (for example, at 2Θ = 17º and 34º) that do not correspond to the mentioned phases and the incommensurable phase of $KSm(MoO_4)_2$. They are neither oxides nor molybdates: $K_2(MoO_4)_3$ and $Tb_2(MoO_4)_3$ (α or β phases). The high-temperature phase with the structure of $RbPr(MoO_4)_2$ (RbPr_hkl in Fig.21) was identified, but a Le Bail refinement was necessary to ensure this.

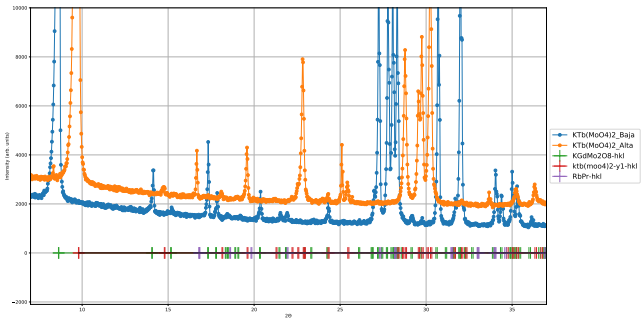

Fig. 21: Diffractograms of $KTb(MoO_4)_2$ (raw data) synthesized at high (orange diffractogram) and low (blue diffractogram) temperature. The bars correspond to the Bragg reflections of the phases α-$KEu(MoO_4)_2$, γ-$KY(MoO_4)_2$ and $RbPr(MoO_4)_2$

X. Le Bail Refinement.

a. Basis of the Le Bail Refinement.

The low resolution of the diffractograms (diffractograms with little or incomplete statistics), prevented us a Rietveld refinement [38], where: 1) the lattice parameters, 2) the profile and width of the peaks and 3) the structure (atomic parameters) are refined by least-squares from the phases found in the bibliography. Consequently, the Le Bail method was used [39], which requires fewer parameters to refine since it is unnecessary to know the crystalline structure. In this case, the intensity in cycle n + 1 is calculated from the intensity of the previous cycle n.

$$I_c^{1+n}(H) = \sum_i I_c^n(H)\,\Omega(2\Theta_i)\left[\frac{y_o^n(2\Theta_i) - y_b^n(2\Theta_i)}{y_c^n(2\Theta_i) - y_b^n(2\Theta_i)}\right] \quad (5)$$

Where $I_c^{1+n}(H)$ is the calculated intensity (integrated area) of the Bragg peak in cycle n + 1 corresponding to the vector H; $I_c^n(H)$ is the intensity calculated from the

same peak in the previous cycle; $\Omega(2\Theta_i)$ is the profile function at the angle $2\Theta_i$. Furthermore, the quotient between brackets is the difference between the observed intensity and the background, divided by the difference between the calculated intensity and the background. Therefore, the first value of $I_c^0(H)$ is required before starting the first cycle of refinement. There is an instruction with which the Fullprof software [40] generates these first intensities. We have to enter the initial lattice parameters from the database. We calculate the background by linear interpolation of points chooses at the base of the diffractogram.

The modified Pseudo-Voigt function of Thompson-Cox and Hastings (with corrections for the axial divergence) is used for the profile function [$\Omega(2\Theta_i)$] refinement [41]. This function considers the broadening due to microstrain and grain or domain size. For this type of function, the shape Ω and its width β of the profile are a mixture of Gaussian and Lorentzian functions and their widths (L and G subindex, respectively):

$$\Omega(2\Theta,\beta) = \eta * L(2\Theta,\beta_L) + (1-\eta) * G(2\Theta,\beta_G) \quad (6)$$

$$\beta_L = X * cos(\Theta) + Y * tan(\Theta) + Z \quad (7)$$

$$\beta_G^2 = P * cos(2\Theta) + U * tan(2\Theta) + V * tan(\Theta) + W \quad (8)$$

The parameters X, Y, Z, P, U, V and W can be refined. The parameter U gives direct information about the microstrains. The parameter X gives direct information about the sizes of the grain or its domains with the same dependence of the angle Θ in the Scherrer formula [42]. The parameter Y has a similar dependency on the angle Θ to the parameter U, which can have information about the grain sizes, although it is more difficult to deduce. Remainder parameters are related to the instrumental resolution. We started from parameters calculated in refinements of previous diffractograms. It is necessary to know the length of the peak base to model the profile function. This length is given by the parameter "wdt" in Fullprof (number of times the peak width at half-height).

Least squares refinement is an iterative process in which the calculated diffractogram (values of $y_{ic}(2\Theta_i)$ has to be adjusted to the observed one (experimental values $y_{io}(2\Theta_i)$, always subtracting the background. The parameters that define the model are refined until convergence is reached. The sum is applied to all the data points of the diffraction pattern:

$$S = \sum_{i=1}^{N} [y_o(2\Theta_i) - y_c(2\Theta_i)]^2 \quad (9)$$

We can determine the agreement obtained by final inspection of the refined diffractograms, qualitatively, where we compare the calculated patterns (y_c) with the observed ones (y_o). In addition, a set of conventional R factors is used (see Table 6) to know more quantitatively this agreement since, with these values, we can compare our refinements and other similar found in the bibliography. In the table, N is the total number of points in the pattern minus the total number of excluded points; P is the number of refined parameters; C is the number of strict constraint functions; N - P + C corresponds to the number of degrees of freedom.

TABLE 6: Rietveld-Le Bail Refinement Agreement Factors [38]

- The profile R_p

$$R_p = 100 * \frac{\sum_i |y_o - y_c|}{\sum_i |y_o|} \quad (10)$$

- The weighted profile R_{wp}

$$R_{wp} = 100 * \left[\frac{\sum_i |y_o - y_c|^2}{\sum_i |y_o|^2}\right]^{\frac{1}{2}} \quad (11)$$

- Expected value R_{exp}

$$R_{exp} = 100 * \left[\frac{N - P + C}{\sum_i (w_i \times y_{oi})^2}\right]^{\frac{1}{2}} \quad (12)$$

- Goodness of fit χ^2

$$\chi^2 = \left(\frac{R_{wp}}{R_{exp}}\right)^2 \quad (13)$$

- integrated intensities R_{Bragg}

$$R_{Bragg} = 100 * \frac{\sum_k |I_k - y_{ck}|}{\sum_k |I_k|} \quad (14)$$

- The structure factors R_F

$$R_F = \frac{\sum_{hkl} |F_{o,hkl}| - |F_{c,hkl}|}{\sum_{hkl} |F_{o,hkl}|} \quad (15)$$

b. Results of the Le Bail Refinement.

The Le Bail refinement of the four phases found is shown in Figs.22-24. The plot in red indicates the observed data ($y_{io}(2\Theta)$), in black the calculated ones ($y_{ic}(2\Theta)$), the difference between them are blue and Bragg reflection are plotted by green lines.

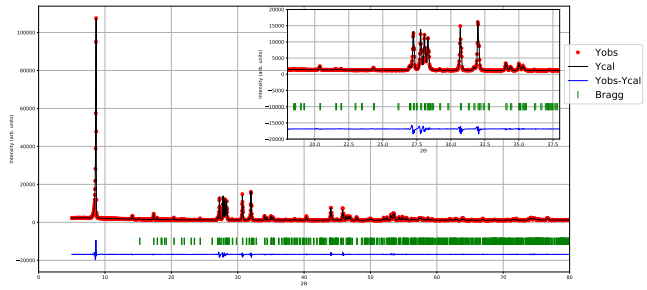

Fig. 22: Refinement of the low-temperature phase of the $KTb(MoO_4)_2$

TABLE 7: Le Bail Refinement parameters obtained.

	$KTb(MO_4)_2$ α-KEu	$KTb(MO_4)_2$ γ-KY	$KTb(MO_4)_2$ RbPr	$KYb(MO_4)_2$ γ-KY
a(Å)	5.267(8)	5.098(6)	6.299(1)	5.042(7)
b(Å)	6.896(7)	18.152(4)	6.437(3)	18.298(5)
c(Å)	10.677(5)	8.017(5)	9.479(3)	7.865(9)
α(º)	75.772(7)	90.000	90.000	90.000
β(º)	76.916(4)	90.000	90.000	90.000
γ(º)	67.445(5)	90.000	90.000	90.000
V(Å3)	343.4(6)	742.0(2)	384.3(8)	725.8(1)
Rp(%)	11,7	10.2	10.2	9.77
Rexp(%)	5,17	4.31	4.31	2.78
X^2	5.15	5.56	5.56	21.2
R_B(%)	1.07	0.566	1.65	0.643

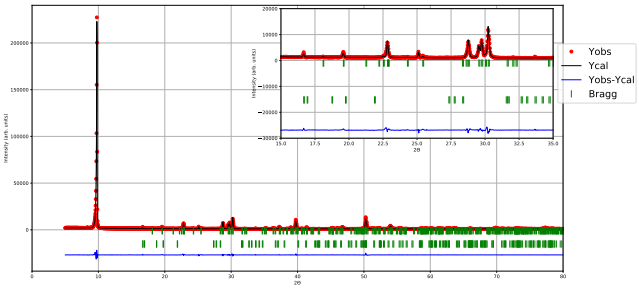

Fig. 23: Refinement of the high-temperature phase of the $KTb(MoO_4)_2$

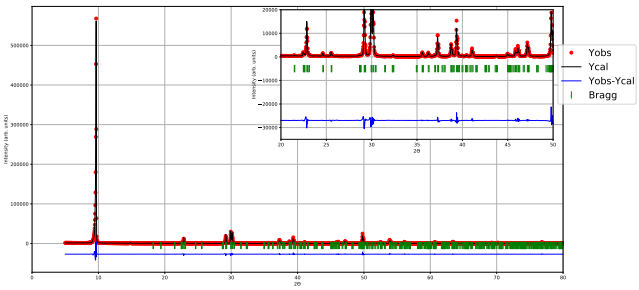

Fig. 24: Refinement of the low-temperature phase of the $KYb(MoO_4)_2$

The result of the refinement is excelent if we consider that we are dealing with routine diffractograms and layered structures. This type of crystal structure presents a broadening of the diffraction peaks (anisotropic and asymmetric). In addition, some of them are displaced due to possible stacking defects. It was solved by adding more refinement parameters to the more intense peak (with an independent Lorentzian width and macrostrain). Even, we found that in some angular ranges it was possible to have peaks with negative width at half-height. This drawback appears in this type of refinement because it is impossible to simulate the intensities of the peaks from the structure factors (therefore, from the atomic positions in a theoretical model). Table 7 shows the result of the refinements.

Fig.22 shows the refinement of the low-temperature $KTb(MoO_4)_2$ phase. It is a pure phase with the structure α-$KEu(MoO_4)_2$, as we identified. The values of the lattice parameters agree with those obtained by other authors very recently [22] and who prepared the sample under similar conditions. The first most intense peak corresponds to the plane (001), where the Tb atoms are located, forming denser layer than other heavy atoms (K and Mo), see Fig.15. This is the expected phase according to the phase diagram shown in Fig.1.

Fig.23 shows the refinement of the high-temperature $KTb(MoO_4)_2$ phase. In addition to the expected phase with structure γ-$KY(MoO_4)_2$, we refine the $RbPr(MoO_4)_2$ phase that appears in the phase diagram (Fig.1). On the other hand, also the same authors who worked with the low-temperature phase [22] obtained a pure phase with the expected high-temperature structure. However, the synthesis procedure was different (flow and melt growth). We do not have references to a complete characterization of this compound prepared by solid-state synthesis. The thermal analysis could help to know the phase changes to achieve the pure phase, probably at lower temperature. We do not have references about the formation of the $RbPr(MoO_4)_2$ phase for this compound, which is feasible for rare earths of higher ionic radius. In this case, the more intense peak corresponds to the plane (020) where the Tb atoms are placed, forming a denser and flatter layer than in the previous case. Therefore, giving rise to a relatively more intense peak than in Fig.22.

Fig.24 show the the refinement of $KYb(MoO_4)_2$ phase. The expected phase was obtained with the structure γ-$KY(MoO_4)_2$. Several satellite peaks and differences in the peak intensities were observed. We think that we have obtained crystals with impurities and more defects than in the previous cases. This phase has also been obtained very recently [23], but the preparation method has not been the same, and it was characterized by single crystal diffraction. Here we also refine with the Le Bail method, although the results were worse than in previous cases. As we have already mentioned, we think that this compound has more defects than the two samples of $KTb(MoO_4)_2$. The phase γ-$KY(MoO_4)_2$ has a clearer layered structure than the phase α-$KEu(MoO_4)_2$, with the distorted scheelite structure (the scheelite structure is not a layered structure). There are more parameters to refine for the second sample and more possibilities to improve the refinement, being a mixture of phases. In fact, the refinements that give better results for layered struc-

tures are based on refining less symmetrical structures or "supercells" in which these defects are simulated, similarly to a phase mixture [43]. In addition, the relative intensity of the first peak (020) with respect to the remaining ones is much higher in this case. The layer of Yb atoms is denser and the distance between layers is also relatively long so stacking defects are possible. We chose to refine the diffractogram that seemed to respond to the most crystalline phase, with fewer impurities and defects (raw data with code M13). We can say that it has been possible to refine, for the first time, diffractograms for this compound prepared by solid-state synthesis. However, we must collect higher resolution diffractograms to perform a more complex Rietveld refinement in which the layer structure can be modeled. A thermal analysis will help to know the range of thermal stability of this compound and if it is possible to sinter a new phase at high temperatura as we see in Fig.1.

XI. Dielectric Properties.

a. Analysis of dielectric spectra: Universal Dielectric Response Model.

The dielectric properties, in particular, the real part of the complex permittivity (ε') and conductivity (σ') of the sample, are studied by measuring the complex impedance Z*(ω). Then, the complex permittivity ($\varepsilon^*(\omega)$) is evaluated from the value obtained from Z*(ω) according to the following relation:

$$\varepsilon^*(\omega) = \frac{e}{i\omega\varepsilon_0 Z^*(\omega)A} \tag{16}$$

Where ε_0 is the dielectric constant of the vacuum, A and e represent the electrode area and the thickness of the sample, respectively. Complex permittivity can be expressed as:

$$\varepsilon^*(\omega) = \varepsilon'(\omega) - i\frac{\sigma'(\omega)}{\omega} \tag{17}$$

Where $\sigma'(\omega)$ is the real part of the frequency-dependent complex conductivity. Analysis of conductivity spectra is based on the Universal Dielectric Response (UDR), an empirical power-law used to describe the frequency dependence in a wide range of disordered materials, including: ionic glasses, non-stoichiometric crystals, polycrystalline or amorphous semiconductors, organic acids, ionic or electronic conductive polymers [44, 45].

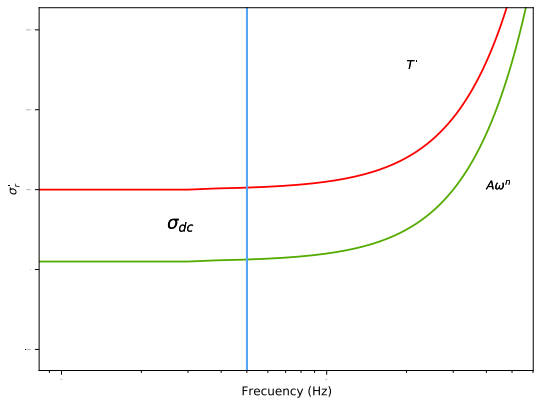

Fig. 25: Variation of the real part of the conductivity, for any two temperatures.

Therefore, the real part of the conductivity spectrum $\sigma'(\omega)$ tends towards direct current conductivity (σ_{dc}) as the frequency decreases and shows a regime dispersive where conductivity increases strongly with frequency (Fig.25). Jonscher proposed the following frequency dependence for conductivity [46]:

$$\sigma'(\omega) = \sigma_{dc} + A\omega^s \tag{18}$$

Where A is a temperature-dependent constant and s is a fractional exponent with a value between 0 and 1. Its value depends on the many-body interactions among the charge carriers. However, in this work, a slightly different version of the above equation is used:

$$\sigma'(\omega) = \sigma_{dc}\left[1 + cos\left(\frac{s\pi}{2}\right)\left(\frac{\omega}{\omega_p}\right)^s\right] \tag{19}$$

Where ω_p (from the real part of the complex conductivity) is defined as a frequency at which occurs a slope change [47]. The temperature dependence of the conductivity factor "σ_{dc}" can be studied by fitting the conductivity values to the previous expressions. For this, the experimental values were adjusted to an Arrhenius-type temperature dependence:

$$\sigma_{dc} = \sigma_0 \cdot exp\left(-\frac{E_a}{K_B T}\right) \tag{20}$$

Where σ_0 is a pre-exponential factor, E_a is the activation energy, and K_B is the Boltzman constant. It is also convenient to analyze the Jonscher parameter s as a function of temperature, this parameter is very sensitive to changes in the ion environment (phase-transitions, distortions of the crystalline structure, decompositions, etc.), which can affect the mobility of charge carriers.

b. Result of the adjustments to the UDR model: Structure-Property Correlation.

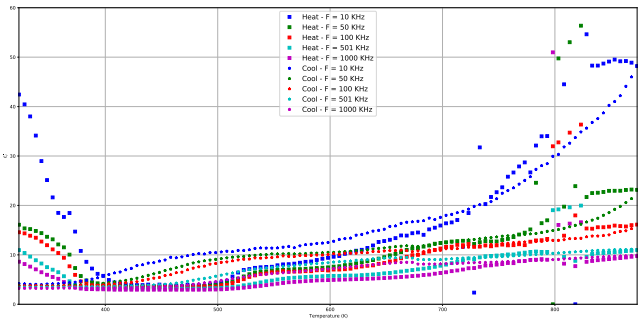

Fig. 26: Real part of the complex dielectric permittivity as a function of temperature, at different frequencies, for a $KTb(Mo0_4)_2$ sample during a heating-cooling cycle.

The variation of the real part of the complex dielectric permitivity (ε'_r) as a function of temperature, at different frequencies, for $KTb(Mo0_4)_2$ is shown in Fig.26. It is observed that the behavior of ε'_r during the heating stage presents some differences with respect to the cooling stage (see also figures in Supplementary information Part VII, Section XVI: Figs. 62 and 63). Both behaviors can be analyzed based on the following three regions:

- Region I (373-498 K), here ε_r' is practically independent of the temperature and the frequency (of the electric field applied during the heating stage).

- Region II (498-623 K), here ε_r' shows a moderate dispersion (moderate variation of the real part of the dielectric permittivity with frequency and temperature) and a broad peak around 533 K, during the heating stage. This peak moves towards higher temperatures, as the frequency increases. A peak with the same characteristics occurs during the cooling stage, but around 488 K. Both phenomena are characteristic of dielectric relaxation processes. Noted that the values of ε_r' during the cooling stage are higher than those of the heating stage. This behavior may be indicative that cation rearrangements have occurred in the crystal structure.

- Region III (623-873 K), the most significant dispersion of ε_r' is shown with a possible "phase-transition" around 823 K. This "phase-transition" is probably not completed, because due to technical limitations of the equipment, the maximum temperature at which the equipment operates is 873 K.

We could expect the transition to phase γ-$KY(MoO_4)_2$ shown in the phase diagram of Fig.1, but the transition temperature is unknown. A dielectric relaxation process is also observed in this region: 1) around 700 K during the heating stage, and 2) around 673 K during the cooling stage.

This dispersion of the real part of the dielectric permittivity leads to changes in electrical conductivity. Thus, in Figs. 27 y 28 the real part of the electrical conductivity is shown ($\sigma'(\omega)$) versus the frequency and the temperature for both stages. It is observed that the conductivity for this material increases with the temperature for a fixed frequency, and also the dependence of the conductivity with the frequency is more remarkable when the temperature increases; therefore the spectra ($\sigma'(\omega)$) are analyzed using the Universal Dielectric Response model. The adjustments to UDR model (Eq.19) are also indicated in Figs. 27 and 28.

As previously mentioned, the dependence of direct current conductivity (σ_{dc}) and the parameter s with temperature can be obtained from these settings. The conductivity values are between 10^{-9} and 10^{-6} S/cm during the heating stage and between $10^{-8.5}$ and $10^{-6.5}$ S/cm during the cooling. The adjustments of the experimental data of ($\sigma'(\omega)$) have been made from 523 K, since ($\sigma'(\omega)$) values for lower temperatures are minimal, being at the limit of sensitivity of the impedance analyzer.

From the settings shown in Figs. 27 and 28, the evolution of the electrical conductivity (σ_{dc}) and the parameter s with the temperature have been obtained (Figs. 29 and 30, respectively) during a heating-cooling cycle.

The dependence of the conductivity, represented as $\ln(\sigma_{dc})$ versus 1000/T, shown in Fig.29, allows to differentiation between two regions with respective activation energies during the activation process. The values of the activation energies,

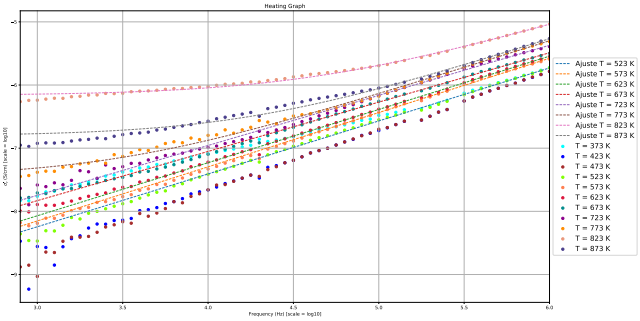

Fig. 27: Real part of the complex electrical conductivity as a function of frequency, at different temperatures, for a sample of $KTb(Mo0_4)_2$ during the heating stage. The dashed lines correspond to the best fits to Eq.19

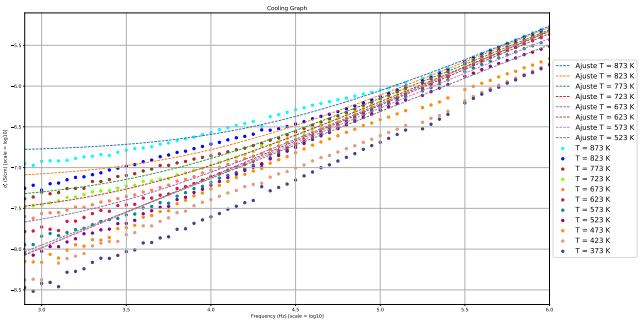

Fig. 28: Real part of the complex electrical conductivity as a function of frequency, at different temperatures, for a sample of $KTb(Mo0_4)_2$ during the cooling stagw. The dashed lines correspond to the best fits to Eq.19

calculated from the different slopes obtained from the adjustment to Eq.20 were, for the heating stage: 0.20 eV (523 K-723 K) and 4.2 eV (723 K - 823 K) and, for the cooling stage: 0.59 eV (873 K - 673 K) and 0.06 eV (623 K- 523 K). The high value of the activation energy (Ea = 4.2 eV), in the interval between 723 and 823 K, during the heating stage can be due to the "phase-transition" (Region III. Fig.26). It was observed in the same temperature range we inspect the curves $\varepsilon_r'(\omega)$. The value of the activation energy equal to 0.59 eV, obtained during the cooling stage, is very close to that obtained by other authors in single crystals of $KTb(Mo0_4)_2$ in the temperature range between 1073 K and 773 K (cooling) [22]. According to them, activation energies values depend on the crystallographic direction in which the data are collected. Thus, they found that for directions *a*, *b* and *c*, the Ea were respectively 0.69, 0.59 and 0.62 eV in the temperature range of 1073 to 773 K. These authors measured the conductivity for the phase γ-$KY(MoO_4)_2$, and they did not observe phase-transition in the experimental temperature range. The small values of activation energies (less than 0.20 eV) observed at low-temperatures are typical of short-range interactions (low barrier heights on the conduction channels) associated with the microstructure. Similar values have been observed in other compounds with a scheelite or related structures [48].

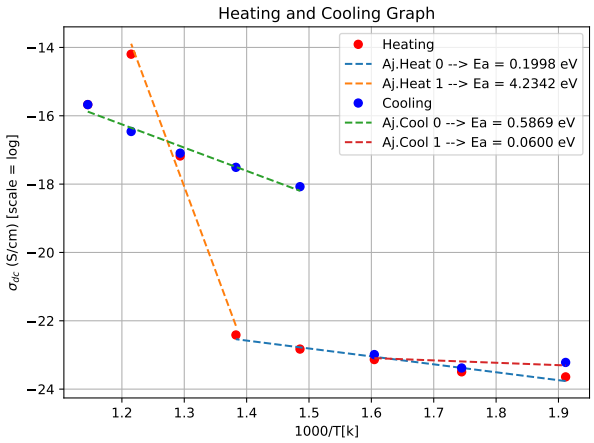

Fig. 29: Dependence of electrical conductivity (σ_{dc}) on temperature for a sample of $KTb(MoO_4)_2$ during a heating-cooling cycle. The dashed lines correspond to the best fits to Eq.20.

The evolution of the parameter s with temperature (Fig.30) also shows differences between the heating and the cooling stages. This parameter is very sensitive to changes in the ion environment (phase-transitions, distortions of the crystalline structure, decompositions, etc.), which can affect the mobility of the charge carriers. Parameter s varies between approximately 0.86 and 0.78 in the temperature range between 523 and 673 K, during the heating stage. That is, there is a slight increase in "disorder" [s = 0, no interaction (Debye model)]. An increase follows this process in the parameter s between approximately 0.78 and 0.85 at 773 K. Both processes cause an increase in conductivity of approximately one order of magnitude ($10^{-8.5}$-$10^{-7.5}$) (Fig.27). This change in the dependence of the parameter s (inflection point around 673 K), may be associated with two processes of different nature. These behaviors are also according to the relaxation phenomena observed in the study of ε_r' (Region II y III) (Fig.26). From 773 K, the value of the parameter s decreases to a value of 0.79 around 823 K, and then increases until 0.86 at 873 K. The minimum conductivity value is obtained at 823 (Fig.27). The variation in conductivity of "almost" one order of magnitude is consistent with the "phase-transition" observed in the study of the dependence of ε_r' (Region III) (Fig.26). The dependence of the parameter s with the temperature between 723 and 823 K can be due to an order-disorder process with high activation energy (Ea = 4.2 eV) (Fig.29). This change would allow the movement of cations from one position to another through the channels, which could explain the increase in conductivity [21]. In Figs. 16a and 16b the zig-zag structure of the channels for the conduction of potassium in phase γ is less pronounced than in phase α, as we have explained in section VIIIb. However, it is necessary to know the complete crystalline structure in both phases to compare the size of these channels quantitatively.

A significant variation of the parameter s during the cooling stage is not observed when the temperature decreases from 873 to 673 K. Therefore, the "phase-transition" at 823 K would be irreversible. Likewise, the parameter s reaches its maximum value of 0.91 at 673 K. Given these results, the higher degree of order of the structure during this stage can be understood. In order to confirm these changes, it would be necessary to have the corresponding X-ray diffraction study with temperature. This study could provide us with information on the variation of the thermal dependence of the lattice parameters and determine the distance between the layers of rare-earth. Thus, we would analyze the viability of the movement of potassium ions through channels, as other authors discussed [22]. In particular, it would be necessary to analyze what happens with the crystal structure around 673 and 823 K during the heating and cooling stage. Finally, because of the mixture of phases obtained by synthesizing $KTb(MoO_4)_2$ at high-temperatures, we expect a rather complex behavior where several phases can coexist at the same temperature. It would explain the thermal hysteresis and other thermal amomalies.

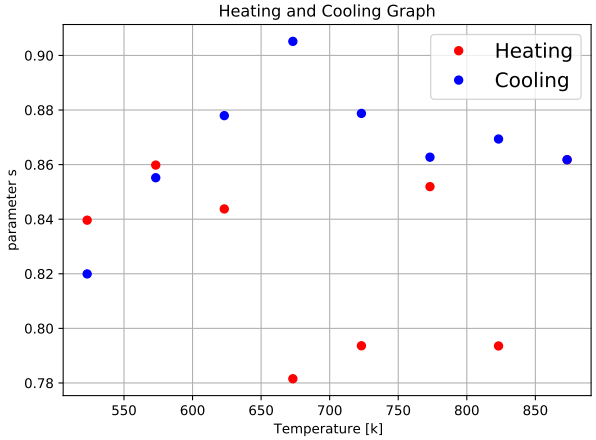

Fig. 30: Dependence of the parameter s with the temperature for a $KTb(Mo0_4)_2$ sample during a heating-cooling cycle.

Part IV
Conclusions

XII. Performed Activities.

Throughout all the time dedicated to the TFM, many different activities have been carried out to complete the objectives set. An extensive bibliography has been consulted, as can be seen in the cited references. In particular, scientific articles related to the crystal structures of double molybdates have been reviewed in considerable depth. Crystal structures have been drawn for comparison. The families of these compounds in which their dielectric properties (especially their conductivity) have also been reviewed.

The compounds $KTb(MoO_4)_2$ and $KYb(MoO_4)_2$ have been prepared with different routes of solid-state synthesis until pure polymorphic phases were obtained. This part was undoubtedly the most difficult to work on because there is not enaugth bibliography on this type of synthesis for these compounds. Therefore, it was a trial and error process to narrow the synthesis conditions.

Phase identification of the synthesized compounds was performed starting from the phase diagram shown in Fig.1.

For $KTb(MoO_4)_2$, two different results were achieved depending on the synthesis temperature. At low-temperature, a pure phase was achieved, and at high-temperature, an unexpected mixture of phases. On the other hand, for $KYb(MoO_4)_2$, a mixture of phases was achieved after many attempts at synthesis. Furthermore, Le Bail method was used for refining the X-ray diffraction patterns. When the pure phases were not achieved, we also refined the mixture of phases. The identification of phases and their refinement was a laborious process when working with powder samples due to the mixing of phases and crystalline defects. The low resolution of the diffractograms prevented us from performing a Rietveld refinement.

For the low-temperature $KTb(MoO_4)_2$ pure phase, dielectric characterization was carried out using impedance spectroscopy as a function of temperature and frequency. We analyzed the possible phase-transitions, relaxation processes and thermal anomalies from the behavior of permittivity and electrical conductivity. The latter was adjusted to the Universal Dielectric Response Model. Thus, continuous conductivity and the Jonscher parameter were calculated as a function of temperature.

XIII. Conclusions.

According to our bibliographical search, the family of $KRE(MoO_4)_2$ compounds is of great technological interest, mainly due to the activity of rare earths in these crystalline matrices. However, no references have been proved explaining its structural variety as a function of synthesis conditions, temperature or pressure, and affecting its optical and electrical properties. As an example, we can say that the phase diagram shown in Fig.1 [13] is practically the same as that from 1977 [49]. We have focused on the compounds $KTb(MoO_4)_2$ and $KYb(MoO_4)_2$ to synthesize and characterize them, coinciding with two publications about them. Concerning the preparation of $KTb(MoO_4)_2$, we have confirmed, thanks to Le Bail refinement, the synthesis conditions for the phase α-$KEu(MoO_4)_2$, recently published. However, the pure γ-$KY(MoO_4)_2$ phase has not been achieved, which has never been synthesized by solid-state reaction to our knowledge. Synthesis conditions must be improved because an unexpected mixture of phases was obtained for rare earth double molybdates with ionic radii shorter than Eu^{3+} radius. These phases were confirmed by Le Bail refinement. About the compound $KYb(MoO_4)_2$, a completely pure crystalline phase, has not been achieved by solid-state synthesis. We have obtained it for the first time. The almost pure γ-$KY(MoO_4)_2$ phase was confirmed by Le Bail refinement. In the recent article, it was obtained by flow growth. Satellite peaks without indexing and anisotropic peak broadening would give information about superstructures caused by stacking defects. Layered structure can lead to this kind of behavior.

Regarding the dielectric study that was only performed for the pure phase of $KTb(MoO_4)_2$, we analyse the real part of the dielectric permittivity (ε_r') as a function of temperature at different frequencies. The heating stage presents some differences with respect to the cooling stage; this is clearly due to the loss of moisture in the sample and which causes variations of the permittivity.

These anomalies were analyzed in three temperature regions. They showed different behaviors according to the temperature and frequency, indicating dielectric relaxation processes and probably even a "phase-transition". In particular, the electrical conductivity spectra fitted to the UDR model obtaining the parameter s and the σ_{dc}, shows differences between the heating and cooling stage. The value of Ea = 0.59 eV, during the cooling stage is within the order of magnitude obtained by other authors on a single crystal of $KTb(Mo0_4)_2$. To confirm the these anomalies, it would be necessary to have the corresponding X-ray diffraction study with temperature, in addition to a thermal analysis study (TG/DSC).

XIV. Future work.

In this work, most of the objectives have been completed with some complications, for instance, the synthesis of $KYb(MoO_4)_2$. Therefore, in future work, it would be convenient to achieve the conditions to obtain the pure phase and to know its thermal stability (including phase-transitions at high temperature) to characterize it dielectrically. In relation to $KTb(MoO_4)_2$, having achieved the conditions for the solid-state synthesis of the phase α-$KEu(MoO_4)_2$, we should also know its thermal stability and their phase-transitions (at least two are expected) to interpret their dielectric properties better. In order to explain the thermal and dielectric behavior of these two compounds, it could carry out the synthesis of other $KRE(MoO_4)_2$(RE = rare-earth element) by the solid-state method and study their thermal stability, phase-transitions and electrical behavior.

It could be approached as a PhD thesis work since this family of compounds presents a great variety of crystalline structures. Research on the structure-optical, electrical, and catalytical properties relationship is fascinating. Although the optical properties are not the aim of our work, they can be studied in depth. These compounds can be used, for instance, as 1) active medium in solid-state lasers, 2) as phosphors in monochromatic and white light LEDs depending on the rare earth used or the combination of them. 3) devices that take advantage of up-/down conversion processes.

Part V
Acknowledgment

I would like to express my gratitude to my supervisors Manuel and Cristina for helping me develop the TFM. They have taught me the synthesis method, perform dielectric measurements, and handle the different programs to study the results. Still, above all, I am deeply grateful for their availability to solve many doubts that made me progress. Also, they gave me the freedom to work independently when I already knew to manage the equipment. I would also like to thank Gerardo, the PhD student of my supervisors, for his dedication, helping me explaining me some details to consider in the experiments. He made my time

in the lab more enjoyable, laughing over some conversations.

I could not forget about my family, who is always there for whatever it takes, especially my parents and brother. They continued to bear with patience another year to keep studying and asked: "What about the f***ing TFM?" For 20 thousand times, I have answered them, hahaha.

Last but not least, my friends, who keep saying "study more..., don't you know enough? They provide me with the balance between studying/working and enjoy life: go to the beach, the mountains, parties, etc. Even going out for a drink is enough. The important thing is to make the most of your time.

> El ayer es historia,
> el mañana es un misterio,
> pero el hoy es un obsequio;
> por eso se llama presente.
>
> (MAESTRO OOGWAY. KUNG FU PANDA (2008))

Part VI
References

[1] A. Laref, *Polarons*. Nova Science Publishers, Incorporated, 2018. [Online]. Available: https://novapublishers.com/shop/polarons-recent-progress-and-perspectives/

[2] H. Kato, N. Matsudo, and A. Kudo, "Photophysical and photocatalytic properties of molybdates and tungstates with a scheelite structure," *Chemistry Letters - CHEM LETT*, vol. 33, pp. 1216–1217, 09 2004. [Online]. Available: https://doi.org/10.1246/cl.2004.1216

[3] V. A. Isupov, "Binary molybdates and tungstates of monoand trivalent elements as possible ferroelastics and ferroelectrics," *Ferroelectrics*, vol. 321, no. 1, pp. 63–90, 2005. [Online]. Available: https://doi.org/10.1080/00150190500259699

[4] R. C. S. Júnior, A. E. Nogueira, A. S. Giroto, J. A. Torres, C. Ribeiro, and K. P. Siqueira, "Microwave-assisted synthesis of ca1-xmnxmoo4 (x = 0, 0.2, 0.7, and 1) and its application in artificial photosynthesis," *Ceramics International*, vol. 47, no. 4, pp. 5388–5398, 2021. [Online]. Available: https://www.sciencedirect.com/science/article/pii/S027288422033162X

[5] V. A. Morozov, A. V. Arakcheeva, P. Pattison, K. W. Meert, P. F. Smet, D. Poelman, N. Gauquelin, J. Verbeeck, A. M. Abakumov, and J. Hadermann, "Keu(moo4)2: Polymorphism, structures, and luminescent properties," *Chemistry of Materials*, vol. 27, no. 16, pp. 5519–5530, 2015. [Online]. Available: https://doi.org/10.1021/acs.chemmater.5b01622

[6] A. Arakcheeva, P. Pattison, G. Chapuis, M. Rossell, A. Filaretov, V. Morozov, and G. Van Tendeloo, "$KSm(MoO_4)_2$, an incommensurately modulated and partially disordered scheelite-like structure," *Acta Crystallographica Section B*, vol. 64, no. 2, pp. 160–171, Apr 2008. [Online]. Available: https://doi.org/10.1107/S0108768108001870

[7] T. Wu, Y. Liu, Y. Lu, L. Wei, H. Gao, and H. Chen, "Morphology-controlled synthesis, characterization, and luminescence properties of keu(moo4)2 microcrystals," *CrystEngComm*, vol. 15, pp. 2761–2768, 2013. [Online]. Available: http://dx.doi.org/10.1039/C3CE27073D

[8] V. A. Morozov, A. V. Arakcheeva, G. Chapuis, N. Guiblin, M. D. Rossell, and G. Van Tendeloo, "Knd(moo4)2: A new incommensurate modulated structure in the scheelite family," *Chemistry of Materials*, vol. 18, no. 17, pp. 4075–4082, 2006. [Online]. Available: https://doi.org/10.1021/cm0605668

[9] Q. Ren, F. Lin, X. Wu, O. Hai, T. Wei, Y. Jiao, and H. Li, "Synthesis and luminescent properties of kgd(moo4)2:sm3+ red phosphor for white light emitting diodes," *Materials Research Bulletin*, vol. 90, pp. 66–72, 2017. [Online]. Available: https://www.sciencedirect.com/science/article/pii/S0025540816319857

[10] F. Cheng, Z. Xia, X. Jing, and Z. Wang, "Li/ag ratio dependent structure and upconversion photoluminescence of li x ag 1- x yb 0.99 (moo 4) 2: 0.01 er 3+ phosphors," *Physical Chemistry Chemical Physics*, vol. 17, no. 5, pp. 3689–3696, 2015.

[11] A. Navrotsky, "Energetic clues to pathways to biomineralization: Precursors, clusters, and nanoparticles," *Proceedings of the National Academy of Sciences*, vol. 101, no. 33, pp. 12 096–12 101, 2004. [Online]. Available: https://www.pnas.org/content/101/33/12096

[12] N. P. Sabalisck, C. Guzmán-Afonso, C. González-Silgo, M. E. Torres, J. Pasán, J. del Castillo, D. Ramos-Hernández, A. Hernández-Suárez, and L. Mestres, "Structures and thermal stability of the α-$LiNH_4SO_4$ polytypes doped with Er^3+ and Yb^3+," *Acta Crystallographica Section B*, vol. 73, no. 1, pp. 122–133, Feb 2017. [Online]. Available: https://doi.org/10.1107/S2052520616019028

[13] A. Volokitina, P. Loiko, E. Vilejshikova, X. Mateos, E. Dunina, A. Kornienko, N. Kuleshov, and A. Pavlyuk, "Eu3+:ky(moo4)2: A novel anisotropic red-emitting material with a layered structure," *Journal of Alloys and Compounds*, vol. 762, pp. 786–796, 2018. [Online]. Available: https://www.sciencedirect.com/science/article/pii/S0925838818319546

[14] N. Anantharamulu, K. K. Rao, G. Rambabu, B. V. Kumar, V. Radha, and M. Vithal, "A wide-ranging review on nasicon type materials," *Journal of materials science*, vol. 46, no. 9, pp. 2821–2837, 2011.

[15] H.-P. Hong, "Crystal structures and crystal chemistry in the system na1+ xzr2sixp3- xo12," *Materials Research Bulletin*, vol. 11, no. 2, pp. 173–182, 1976.

[16] B. Lazoryak and V. Efremov, "Na2x sc2 (1–x)-(moo4) 3 (m= zn, cd, mg) phases of variable composition," *Zh. Neorg. Khim.*, vol. 32, no. 3, pp. 652–656, 1987.

[17] N. Sorokin, "Ionic conductivity of kmgfe (moo 4) 3 crystals," *Inorganic Materials*, vol. 51, no. 5, pp. 490–493, 2015.

[18] J. G. Bazarova, A. V. Logvinova, B. G. Bazarov, Y. L. Tushinova, S. G. Dorzhieva, and J. Temuujin, "Synthesis of new triple molybdates k5rzr (moo4) 6 (r= al, cr, fe, in, sc) in the k2moo4-r2 (moo4) 3-zr (moo4) 2 systems, their structure and electrical properties," *Journal of Alloys and Compounds*, vol. 741, pp. 834–839, 2018.

[19] V. G. Grossman, J. G. Bazarova, M. S. Molokeev, and B. G. Bazarov, "New triple molybdate k5schf (moo4) 6: synthesis, properties, structure and phase equilibria in the m2moo4–sc2 (moo4) 3–hf (moo4) 2 (m= li, k) systems," *Journal of Solid State Chemistry*, vol. 283, p. 121143, 2020.

[20] G. D. Tsyrenova, E. Pavlova, S. F. Solodovnikov, N. N. Popova, T. Y. Kardash, S. Y. Stefanovich, I. Gudkova, Z. A. Solodovnikova, and B. I. Lazoryak, "New ferroelastic k2sr (moo4) 2: Synthesis, phase transitions, crystal and domain structures, ionic conductivity," *Journal of Solid State Chemistry*, vol. 237, pp. 64–71, 2016.

[21] B. Lazoryak and V. Efremov, "On the structure of palmierite-like k 5 nd (moo 4) 4, k 5 bi (moo 4) 4, rb 5 gd (moo 4) 4," *Kristallografiya*, vol. 31, no. 2, pp. 237–243, 1986.

[22] V. A. Morozov, S. M. Posokhova, S. Y. Istomin, D. V. Deyneko, A. A. Savina, B. S. Redkin, N. V. Lyskov, D. A. Spassky, A. A. Belik, and B. I. Lazoryak, "Ktb (moo4) 2 green phosphor with k+-ion conductivity: Derived from different synthesis routes," *Inorganic Chemistry*, 2021.

[23] P. Armand, C. Reibel, D. Granier, and M. Tillard, "Growth, single-crystal structure, and magnetic properties of the double molybdate kyb (moo4) 2," *Journal of Physics and Chemistry of Solids*, vol. 154, p. 110023, 2021.

[24] K. P. Mani, G. Vimal, P. Biju, C. Joseph, N. Unnikrishnan, and M. Ittyachen, "Structural and spectral investigation of terbium molybdate nanophosphor," *Spectrochimica Acta Part A: Molecular and Biomolecular Spectroscopy*, vol. 148, pp. 412–419, 2015.

[25] ULL. Segai. [Online]. Available: https://www.ull.es/servicios/segai/

[26] Wikipedia. Ley de bragg. [Online]. Available: https://es.wikipedia.org/wiki/Ley_de_Bragg

[27] CSIC. Dispersión y difracción. ley de bragg. [Online]. Available: http://www.xtal.iqfr.csic.es/Cristalografia/parte_05_5.html

[28] Wikipedia. Difractómetro. [Online]. Available: https://es.wikipedia.org/wiki/Difract%C3%B3metro

[29] ULL. Sidix. [Online]. Available: https://www.ull.es/servicios/segai/servicios/difraccion-rx/

[30] Wikipedia. Espectroscopia dieléctrica. [Online]. Available: https://es.wikipedia.org/wiki/Espectroscopia_diel%C3%A9ctrica

[31] ——. Ciencia de materiales. [Online]. Available: https://es.wikipedia.org/wiki/Ciencia_de_materiales

[32] H. Marzougui, V. Sánchez, S. León-Luis, A. Lozano-Gorrín, E. Lalla, M. Torres, S. Attia-Essaies, and D. B. Hassen-Chehimi, "Dielectric properties and thermal decomposition of k 2 ni (so 4) 2 crystals," *Journal of Electronic Materials*, vol. 45, no. 11, pp. 5839–5846, 2016.

[33] A. Zalkin and D. H. Templeton, "X-ray diffraction refinement of the calcium tungstate structure," *The Journal of Chemical Physics*, vol. 40, no. 2, pp. 501–504, 1964.

[34] V. A. Morozov, S. M. Posokhova, D. V. Deyneko, A. A. Savina, A. V. Morozov, O. A. Tyablikov, B. S. Redkin, D. A. Spassky, J. Hadermann, and B. I. Lazoryak, "Influence of annealing conditions on the structure and luminescence properties of kgd 1- x eu x (moo 4) 2 (0 x 1)," *CrystEngComm*, vol. 21, no. 42, pp. 6460–6471, 2019.

[35] V. Atuchin, V. Grossman, S. Adichtchev, N. Surovtsev, T. Gavrilova, and B. Bazarov, "Structural and vibrational properties of microcrystalline tlm (moo4) 2 (m= nd, pr) molybdates," *Optical Materials*, vol. 34, no. 5, pp. 812–816, 2012.

[36] F.-K. GmbH. Icsd. [Online]. Available: https://icsd.fiz-karlsruhe.de/index.xhtml;jsessionid=16E5054764514C30867981902A0424CF

[37] T. F. Team. Fullprof suite. [Online]. Available: https://www.ill.eu/sites/fullprof/php/reference.html

[38] R. Young, "The rietveld method, international union of crystallography monographs on crystal and oxford science publications," 1995.

[39] A. Le Bail, "Whole powder pattern decomposition methods and applications: A retrospection," *Powder diffraction*, vol. 20, no. 4, pp. 316–326, 2005.

[40] T. F. Team. Fullprof suite. [Online]. Available: http://www.ill.eu/sites/fullprof/

[41] R. E. Dinnebier and S. J. Billinge, "Principles of powder diffraction," *Powder Diffraction: Theory and Practice*, pp. 1–19, 2008.

[42] A. Patterson, "The scherrer formula for x-ray particle size determination," *Physical review*, vol. 56, no. 10, p. 978, 1939.

[43] A. A. Coelho, J. S. Evans, and J. W. Lewis, "Averaging the intensity of many-layered structures for accurate stacking-fault analysis using rietveld refinement," *Journal of Applied Crystallography*, vol. 49, no. 5, pp. 1740–1749, 2016.

[44] A. K. Jonscher, "The 'universal'dielectric response," *nature*, vol. 267, no. 5613, pp. 673–679, 1977.

[45] K. Ngai, A. Jonscher, and C. White, "On the origin of the universal dielectric response in condensed matter," *Nature*, vol. 277, no. 5693, pp. 185–189, 1979.

[46] A. Jonscher, "Dielectric relaxation in solids, chelsea," *Dielectrics Pub., London*, 1983.

[47] C. León, M. Lucia, and J. Santamaria, "Correlated ion hopping in single-crystal yttria-stabilized zirconia," *Physical Review B*, vol. 55, no. 2, p. 882, 1997.

[48] R. Venkatesan, S. Velumani, M. Tabellout, N. Errien, and A. Kassiba, "Dielectric behavior, conduction and epr active centres in bivo4 nanoparticles," *Journal of Physics and Chemistry of Solids*, vol. 74, no. 12, pp. 1695–1702, 2013.

[49] P. Klevtsov and R. Klevtsova, "Polymorphism of the double molybdates and tungstates of mono-and trivalent metals with the composition m+ r 3+(eo 4) 2," *Journal of Structural Chemistry*, vol. 18, no. 3, pp. 339–355, 1977.

Part VII
Supplementary information

XV. $KYb(MoO_4)_2$ synthesis experiences.

Adjusted equations and quantities for preparing 1g of $KYb(MoO_4)_2$ is explained in detail in section a. The different experiences gave us information on which parameters could be varied to obtain the phase. When carrying out the different experiences and comparing with the theoretical diffractogram, it was concluded that it was necessary:

-use an extra percentage of K_2CO_3, going from 20% to 30%.

-perform the precalcination of theK_2CO_3 with a different heat treatment (see Fig.6).

a. Experience 1.

TABLE 8: Amounts of reagents required.

Reactives	Extra percentage (%)	Final Mass (g)
MoO_3	10	0.5952
K_2CO_3	20	0.1559
Yb_2O_3	10	0.4074

The required amount of reagents is weighed (after Precalcination, following the heat treatments shown in Figs. 4 and 31.).

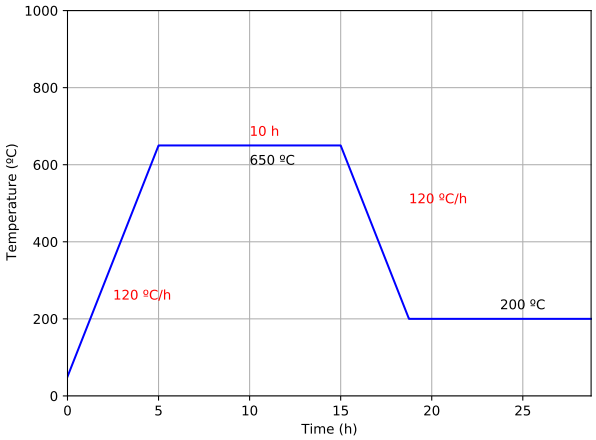

Fig. 31: Precalcination of reactives MoO_3 and K_2CO_3.

Samples are then placed in an agate mortar and ground for at least 1.5 hours so that the mixture is homogeneous as possible. Pellets are made with the ground powder to increase the contact surface between the grains, thus favoring the solid-state reaction. And then the pellets are placed in a platinum crucible and subjected to a heating/cooling program (Heat treatment in Fig.32).

The process is then supervised by X-ray Diffraction obtaining the diffractogram of Fig.33.

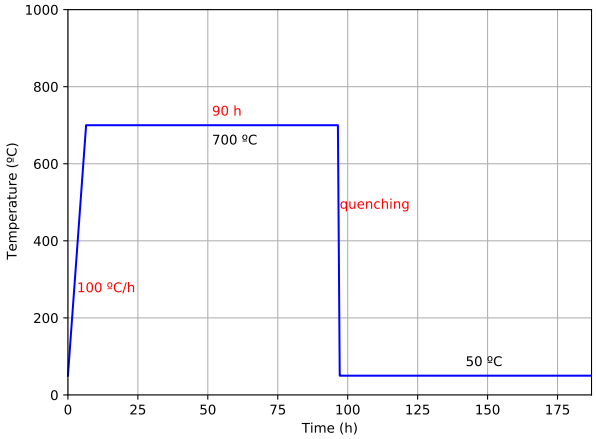

Fig. 32: Heat treatment.

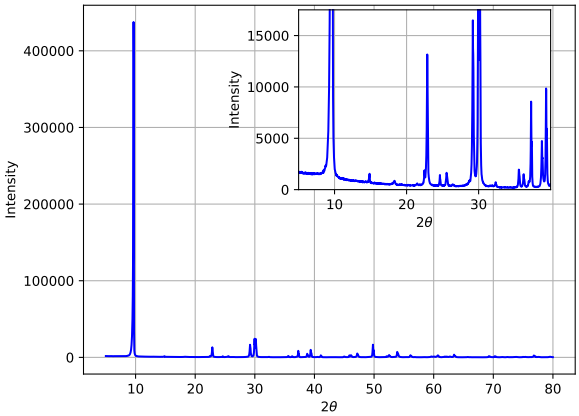

Fig. 33: Diffractogram sample M0a.

b. Experience 2.

Using the pellet from the previous experience, it was grounded in an agate mortar and then placed in the oven because impurity peaks remained in the diffractograms. The pellet is made with the ground powder and the pellet is placed in a platinum crucible and subjected to a heating/cooling program. (Heat treatment in Fig.34). See the diffractogram of Fig.35.

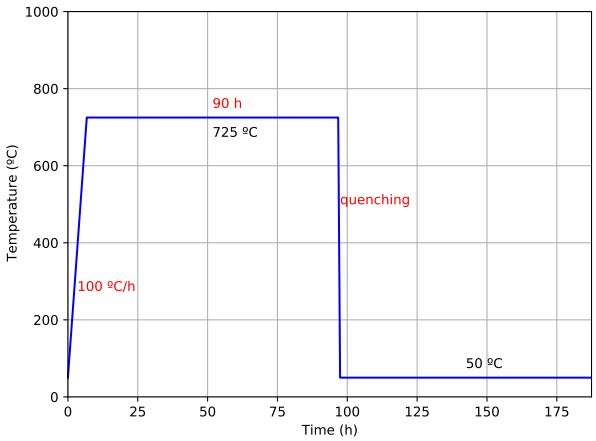

Fig. 34: Heat treatment.

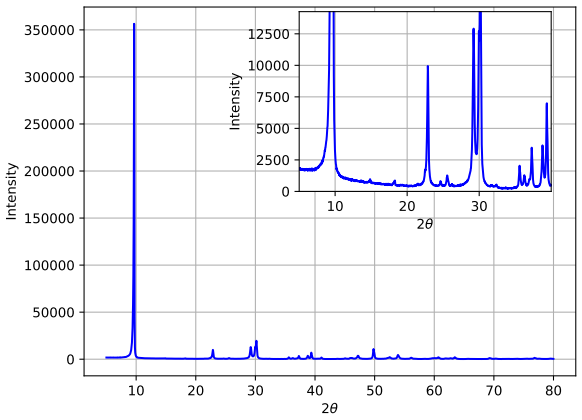

Fig. 35: Diffractogram sample M0b.

c. Experience 3.

TABLE 9: Amounts of reagents required.

Reactives	Extra percentage (%)	Final Mass (g)
MoO_3	10	0.5952
K_2CO_3	20	0.1559
Yb_2O_3	10	0.4074

The necessary amount of reagents were weighed (after Precalcination, following the heat treatments shown in Figs. 4 and 31). Then they are grounded in an agate mortar. Then, the pellets were made to obtain the phase. We decided to perform two different heat treatments (Figs. 36 and 37).

TABLE 10: Number of treatments

Compound	Pressure (ton)	Temperature (ºC)
M1	3	680
M2	3	680
M3	5	725
M4	5	725

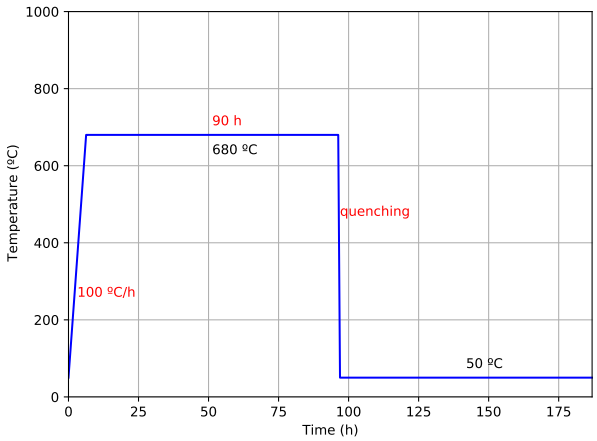

Fig. 36: Heat treatment for M1 and M2.

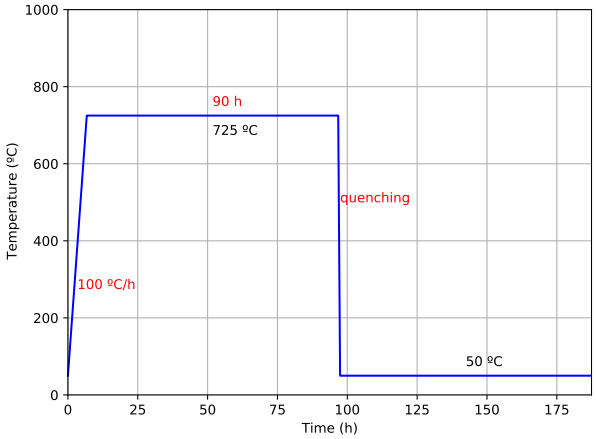

Fig. 37: Heat treatment for M3 and M4.

The process is then monitored by X-ray Diffraction, obtaining the diffractogram of Fig 38, 39, 40 and 41.

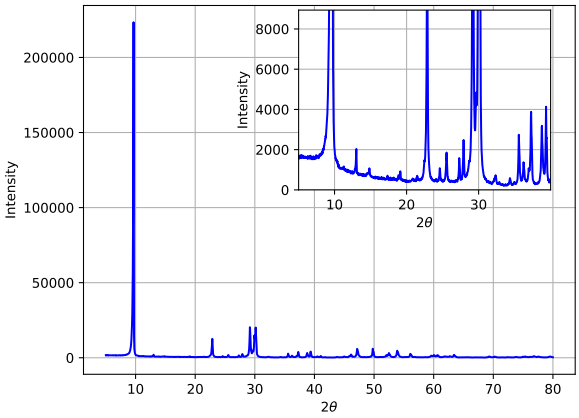

Fig. 38: Diffractogram sample M1.

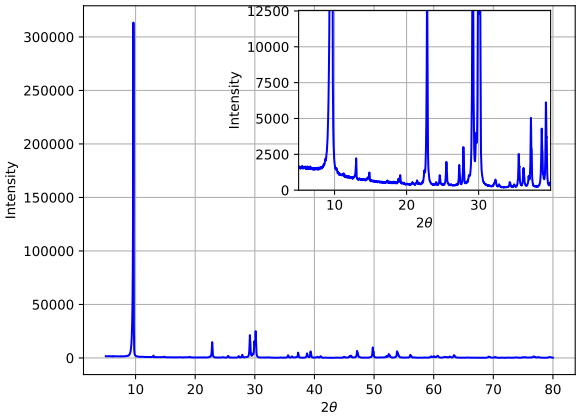

Fig. 39: Diffractogram sample M2.

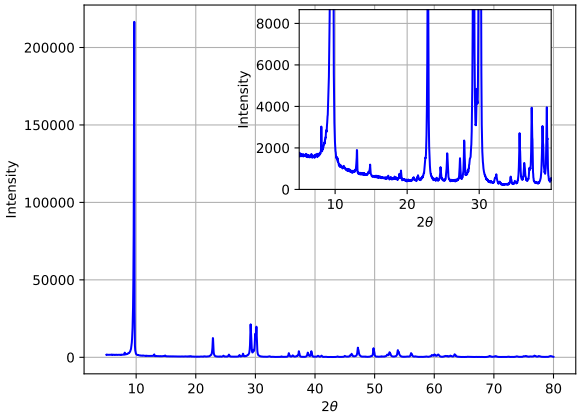

Fig. 40: Diffractogram sample M3.

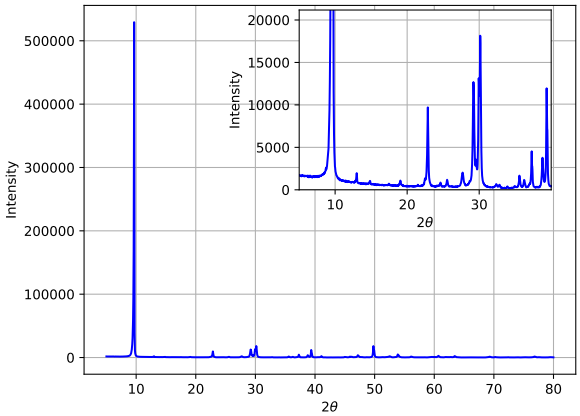

Fig. 41: Diffractogram sample M4.

d. Experience 4.

TABLE 11: Amounts of reagents required.

Reactives	Extra percentage (%)	Final Mass (g)
MoO_3	10	0.5952
K_2CO_3	30	0.16887
Yb_2O_3	10	0.4074

The required amount of reagents is weighed (after Precalcination, following the heat treatments shown in Figs. 4, 5 and 6). Then, they are grounded in an agate mortar. The pellets were made to obtain the phase. We decided to perform two different heat treatments (Figs. 42 and 43).

TABLE 12: Number of treatments

Compound	Pressure (ton)	Temperature (ºC)
M5	3	680
M6	5	680
M7	3	750
M8	5	750

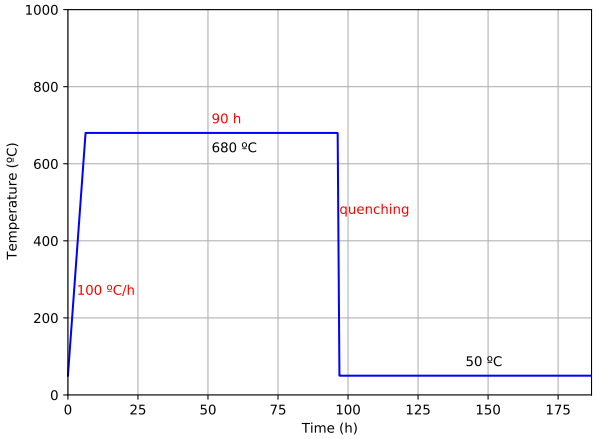

Fig. 42: Heat treatment for M5 and M6.

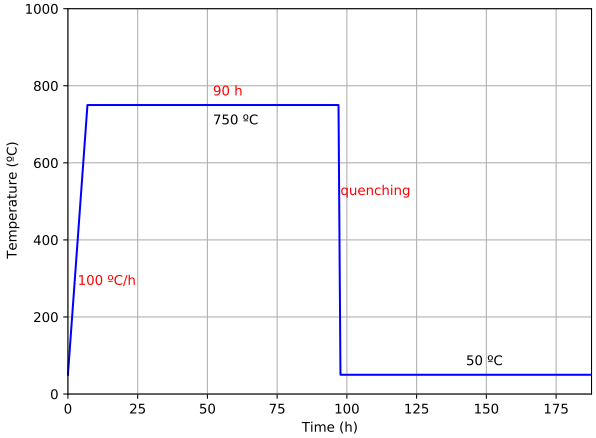

Fig. 43: Heat treatment for M7 and M8.

The process is then monitored by X-ray Diffraction obtaining the diffractogram of Fig 44, 45, 46 and 47.

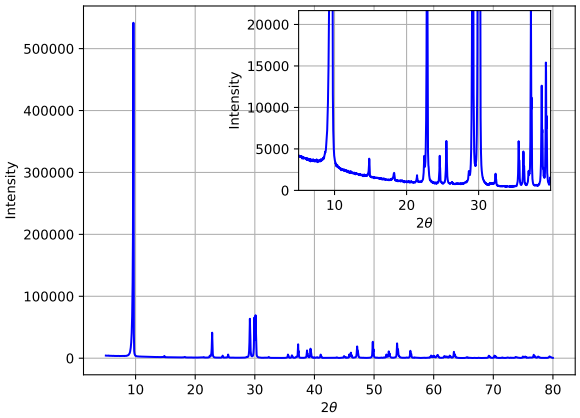

Fig. 44: Diffractogram sample M5.

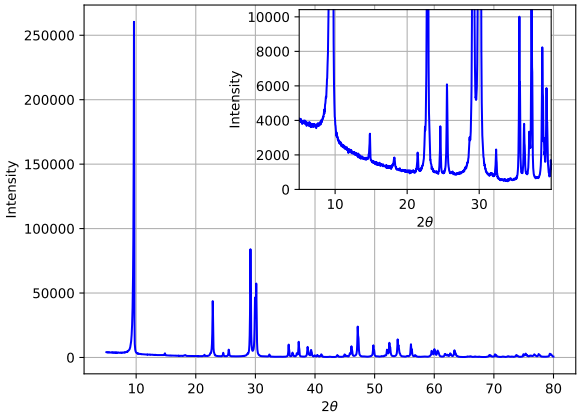

Fig. 45: Diffractogram sample M6.

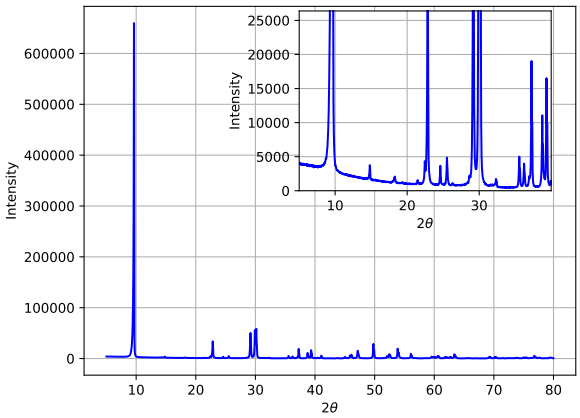

Fig. 46: Diffractogram sample M7.

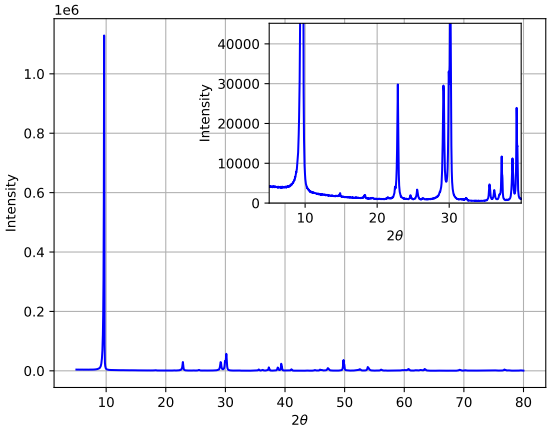

Fig. 47: Diffractogram sample M8.

e. Experience 5.

TABLE 13: Amounts of reagents required.

Reactives	Extra percentage (%)	Final Mass (g)
MoO_3	10	0.5952
K_2CO_3	30	0.16887
Yb_2O_3	10	0.4074

The required amount of reagents is weighed (after Precalcination, following the heat treatments shown in Figs. 4, 5 and 6). Then, samples are grounded in an agate mortar. Pellets were made to obtain the phase. We decided to perform three different heat treatments (Figs. 48, 49 and 50).

TABLE 14: Number of treatments

Compound	Pressure (ton)	Temperature (ºC)	Tiempo (h)
M9	3	625	90
M10	5	625	90
M11	3	650	90
M12	3	625	60

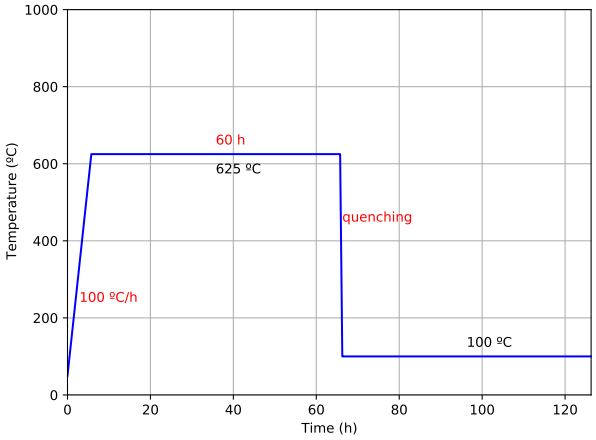

Fig. 50: Heat treatment for M12.

The process is then monitored by X-ray Diffraction obtaining the diffractogram of Fig 51, 52, 53 and 54.

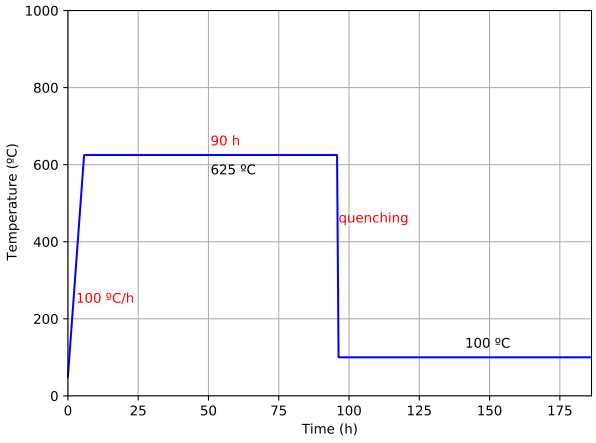

Fig. 48: Heat treatment for M9 and M10.

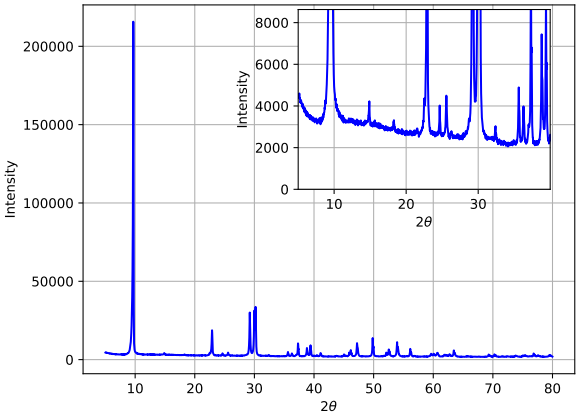

Fig. 51: Diffractogram sample M9.

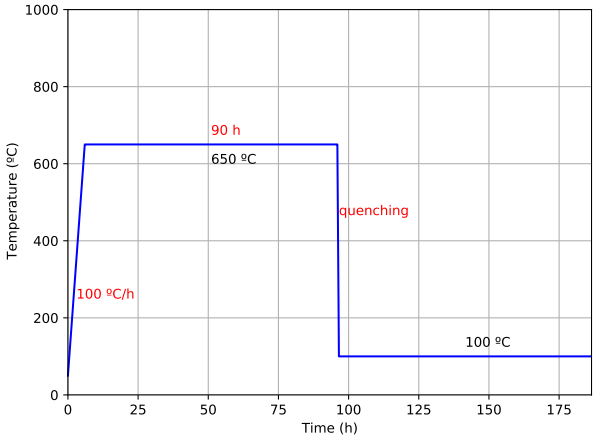

Fig. 49: Heat treatment for M11.

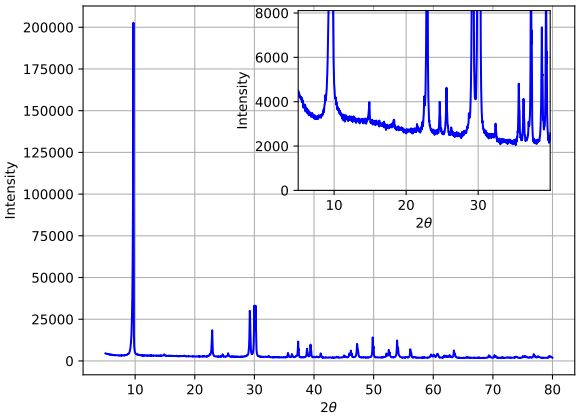

Fig. 52: Diffractogram sample M10.

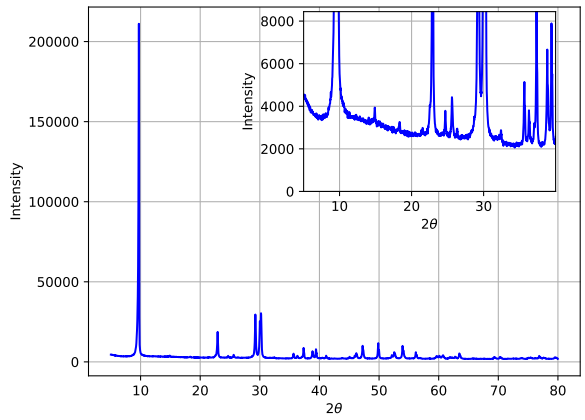

Fig. 53: Diffractogram sample M11.

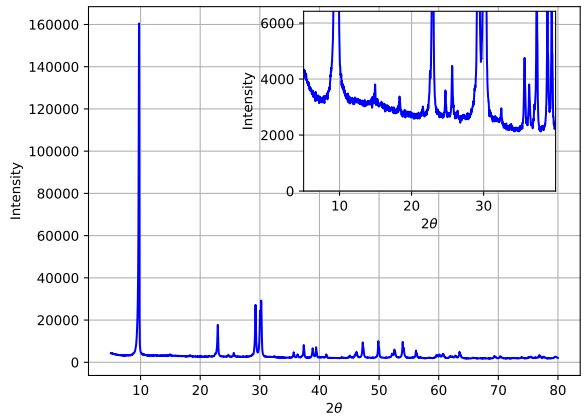

Fig. 54: Diffractogram sample M12.

f. Experience 6.

TABLE 15: Amounts of reagents required.

Reactives	Extra percentage (%)	Final Mass (g)
MoO_3	10	0.5952
K_2CO_3	30	0.16887
Yb_2O_3	10	0.4074

The required amount of reagents is weighed (after Precalcination, following the heat treatments shown in Figs. 4, 5 and 6). Then, they are grounded in an agate mortar. Then, pellets were made to obtain the phase. We decided to do three different heat treatments (Figs. 55, 56 and 57).

TABLE 16: Number of treatments

Compound	Pressure (ton)	Temperature (ºC)	Tiempo (h)
M13	3	690	90
M14	3	700	90
M15	3	710	90

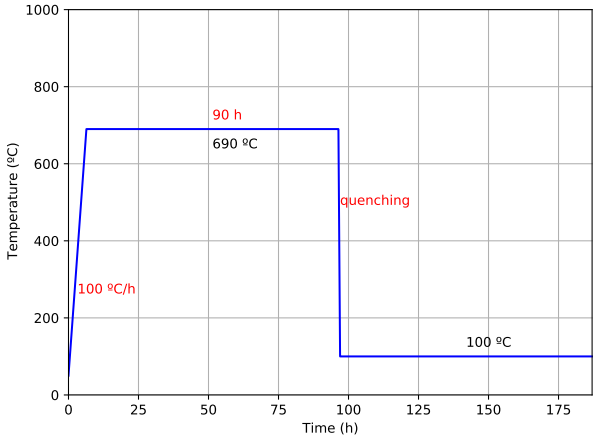

Fig. 55: Heat treatment for M13.

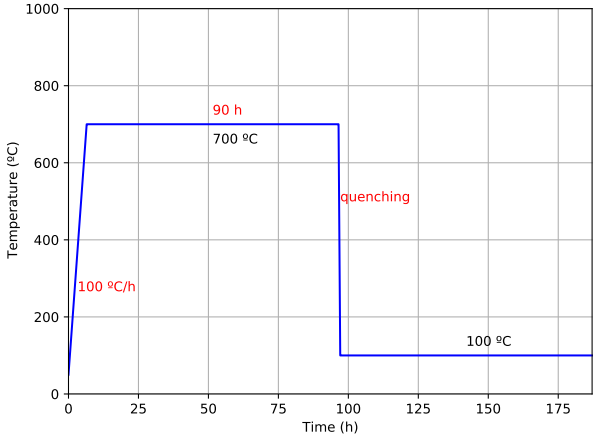

Fig. 56: Heat treatment for M14.

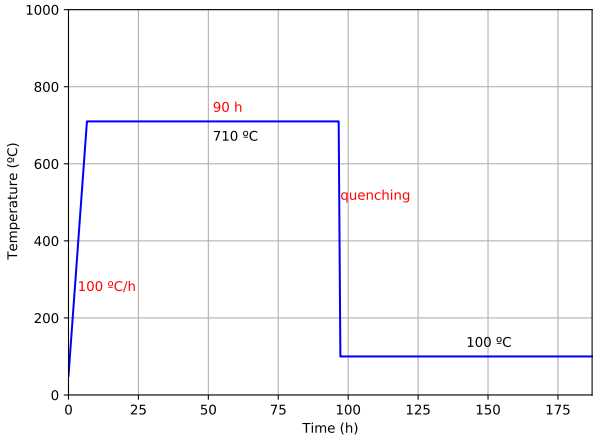

Fig. 57: Heat treatment for M15.

Then it should be taken to the SIDIX to monitor the process by X-ray Diffraction, this was impossible since the service had closed, but given that the procedure is the same we should have obtained the same (although we can not affirm with certainty, the X-ray Diffraction is necessary). After starting with Experience 7, the X-ray results of the samples arrived, obtaining the diffractogram of Figs. 58, 59 and 60

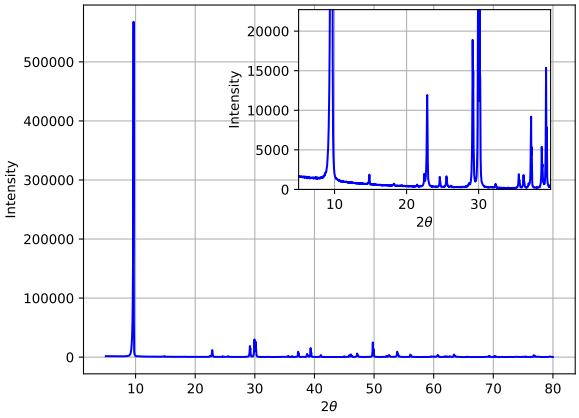

Fig. 58: Diffractogram sample M13.

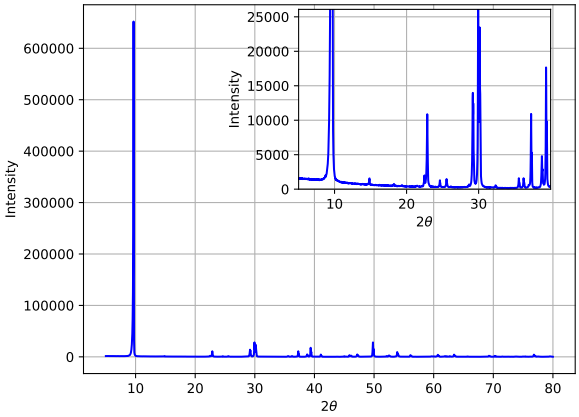

Fig. 59: Diffractogram sample M14.

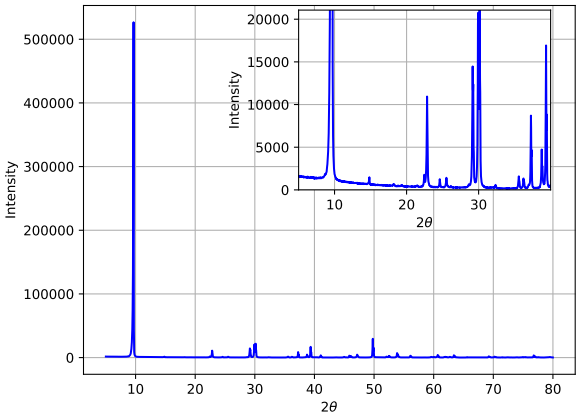

Fig. 60: Diffractogram sample M15.

g. Experience 7.

After a review of the multiple diffractograms and in the absence of knowing the results of Experience 6, we concluded that the best result was M6 (obtained in Experience 4), since its diffractogram is a mixture of phases, the $KY(MoO_4)_2$ and $Y_2(MoO_4)_3$. The same procedure as in Experiment 4 is followed, obtaining the diffractogram of Fig.61.

TABLE 17: Amounts of reagents required.

Reactives	Extra percentage (%)	Final Mass (g)
MoO_3	10	0.5952
K_2CO_3	30	0.16887
Yb_2O_3	10	0.4074

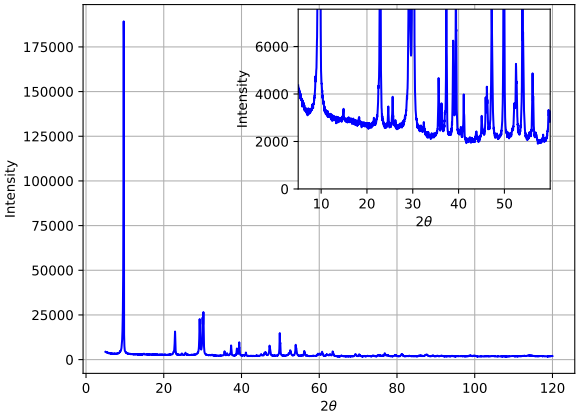

Fig. 61: Diffractogram sample M6.

XVI. Impedance Measurement Graphs.

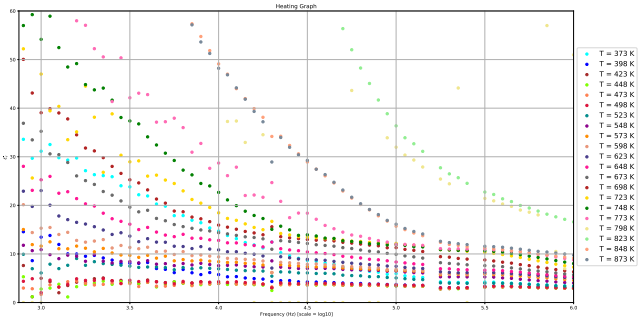

Fig. 62: Real part of the complex dielectric permittivity as a function of frequency, at different temperatures, for a sample of $KTb(Mo0_4)_2$ during the heating stage.

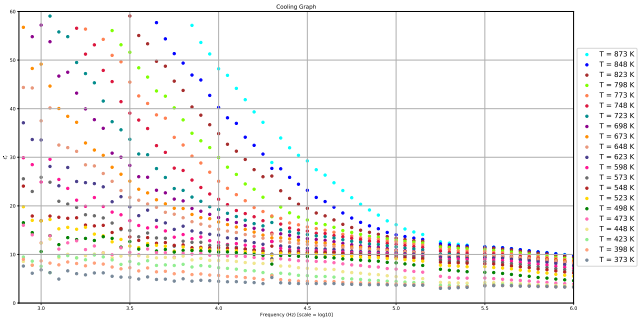

Fig. 63: Real part of the complex dielectric permittivity as a function of frequency, at different temperatures, for a sample of $KTb(Mo0_4)_2$ during the cooling stage.